INTERACTING COSMIC RAYS WITH MOLECULAR CLOUDS: A BREMSSTRAHLUNG ORIGIN OF DIFFUSE HIGH-ENERGY EMISSION FROM THE INNER 2° × 1° OF THE GALACTIC CENTER

F. Yusef-Zadeh[1], J. W. Hewitt[2], M. Wardle[3], V. Tatischeff[4], D. A. Roberts[1], W. Cotton[5],
H. Uchiyama[6], M. Nobukawa[6], T. G. Tsuru[6], C. Heinke[7], AND M. Royster[1]

[1] Department of Physics and Astronomy, Northwestern University, Evanston, IL 60208, USA
[2] Code 662, NASA Goddard Space Flight Center, Greenbelt, MD 20771, USA
[3] Department of Physics & Astronomy, and Research Center for Astronomy, Astrophysics & Astrophotonics, Macquarie University, Sydney, NSW 2109, Australia
[4] Center de Spectrométrie Nucléaire et de Spectrométrie de Massse, IN2P3/CNRS and Univ. Paris-Sud, F-91405 Orsay Campus, France
[5] NRAO, 520 Edgemont Road, Charlottesville, VA 22903, USA
[6] Cosmic Ray Group, Physics, Kyoto University, Kitashirakawa-Oiwake-Cho, Sakyo, Kyoto 606-8502, Japan
[7] Department of Physics, Room 238 CEB, University of Alberta, Edmonton, AB T6G 2G7, Canada
Received 2012 June 8; accepted 2012 October 31; published 2012 December 13

ABSTRACT

The high-energy activity in the inner few degrees of the Galactic center is traced by diffuse radio, X-ray, and γ-ray emission. The physical relationship between different components of diffuse gas emitting at multiple wavelengths is a focus of this work. We first present radio continuum observations using the Green Bank Telescope and model the nonthermal spectrum in terms of a broken power-law distribution of $\sim$GeV electrons emitting synchrotron radiation. We show that the emission detected by *Fermi* is primarily due to nonthermal bremsstrahlung produced by the population of synchrotron emitting electrons in the GeV energy range interacting with neutral gas. The extrapolation of the electron population measured from radio data to low and high energies can also explain the origin of Fe I 6.4 keV line and diffuse TeV emission, as observed with *Suzaku*, *XMM-Newton*, *Chandra*, and the H.E.S.S. observatories. The inferred physical quantities from modeling multiwavelength emission in the context of bremsstrahlung emission from the inner $\sim$300 × 120 pc of the Galactic center are constrained to have the cosmic-ray ionization rate $\sim$1–10 × 10^{-15} s^{-1}, molecular gas heating rate elevating the gas temperature to 75–200 K, fractional ionization of molecular gas 10^{-6}–10^{-5}, large-scale magnetic field 10–20 μG, the density of diffuse and dense molecular gas $\sim$100 and $\sim$$10^3$ cm^{-3} over 300 pc and 50 pc path lengths, and the variability of Fe I Kα 6.4 keV line emission on yearly timescales. Important implications of our study are that GeV electrons emitting in radio can explain the GeV γ-rays detected by *Fermi* and that the cosmic-ray irradiation model, like the model of the X-ray irradiation triggered by past activity of Sgr A*, can also explain the origin of the variable 6.4 keV emission from Galactic center molecular clouds.

Key words: cosmic rays – Galaxy: center

Online-only material: color figures

1. INTRODUCTION

The Galactic center hosts several sources of energetic activity: X-ray flare activity from Sgr A*, nonthermal linear filaments, supernova remnants interacting with molecular clouds, colliding winds of massive stars, pulsars, transient radio and X-ray sources, and a population of hard X-ray sources (Muno et al. 2006, 2009; Koyama et al. 1996; Tsuboi et al. 1997; Baganoff et al. 2001; Murakami et al. 2001; Deneva et al. 2009). This region also hosts massive molecular clouds containing pockets of current and past massive star formation (see Jones et al. 2011 and references therein). The most prominent clouds are associated with Sgr B2 and Sgr C, the 50, 40, 20, and −30 km s^{-1} complexes as well as the cloud G0.11−0.11 adjacent to the radio continuum Arc near $l \sim 0°.2$. Molecular clouds are traditionally studied by molecular line observations at millimeter wavelengths. However, diffuse high-energy emission has also been detected from Galactic center molecular clouds. These unique Galactic center molecular clouds that emit the 6.4 keV X-ray line, GeV and TeV radiation as well as rotationally excited millimeter lines help to bridge a gap in understanding the radiation processes that operate at low and high energies.

The Galactic center region hosts warm molecular gas as well as a number of synchrotron emitting radio sources. A high cosmic-ray ionization rate is estimated from H$_3^+$ measurements of this region (Oka et al. 2005). It is then natural to consider the interaction of cosmic-ray electrons that produce radio emission with ambient gas in the context of nonthermal bremsstrahlung. We study this interaction in detail and investigate the origin of the high cosmic-ray ionization rate and high molecular gas temperature (Oka et al. 2005; Hüttemeister et al. 1993). We show the distribution of GeV γ-ray emission observed by *Fermi* and model the emission by studying the population of nonthermal electrons using radio data. Furthermore, the extrapolation of the radio spectrum of the GeV population to 10 keV as well as a young population of electrons extrapolated to TeV energies can also explain the observed emission at X-ray and TeV energy range, respectively. In particular, the fluorescent Fe I Kα line emission at 6.4 keV and diffuse TeV emission are recognized to trace the molecular clouds of the Galactic center. It has been suggested that the fluorescent 6.4 keV emission results from X-ray irradiation (Sunyaev et al. 1993). The source of the emission is considered to be a hypothetical transient source associated with the massive black hole at the Galactic center, Sgr A*, and that we are now seeing its echo in the 6.4 keV line emission (Koyama et al. 1996; Murakami et al. 2001; Ponti et al. 2010). This event requires a hard X-ray luminosity of $\sim$$10^{39}$ erg s^{-1} from Sgr A*. The year-to-year time variability of 6.4 keV line emission has also been used as a strong support for the irradiation scenario. In this picture, the yearly variability is

due to X-ray fronts from multiple outbursts from Sgr A* which occurred in the last few hundred years. The origin of the 6.4 keV line emission from neutral iron due to low-energy cosmic-ray (LECR) electrons and protons of neutral gas has also been considered (Yusef-Zadeh et al. 2007b; Chernyshov et al. 2011). More recently, the origin of the 6.4 keV line emission from the Arches cluster has also been explained in terms of cosmic-ray ion bombardment of molecular gas surrounding the cluster (Tatischeff et al. 2012). Here, we reinvestigate the cosmic-ray irradiation picture in the context of nonthermal bremsstrahlung. It is important to determine the 6.4 keV emission contributed by each of these two models as they provide evidence for the past activity of Sgr A* or for a large population of LECRs in the Galactic center region.

We begin by describing radio observations using the Green Bank Telescope (GBT), γ-ray observations with the *Fermi* Large Area Telescope (LAT), and X-ray line observations in Section 2. In Section 2.1, the spectrum of radio emission between 325 MHz and 8.5 GHz is modeled in order to separate thermal and nonthermal radio components. In Section 3, we estimate the cosmic-ray ionization rate and compare it with that measured from H_3^+ absorption lines (Oka et al. 2005; Goto et al. 2011). We also account for the warm molecular gas as observed throughout the Galactic center and the origin of 6.4 keV emission from Galactic center molecular clouds. Sections 2 and 3 discuss the interaction of LECR particles with molecular gas, whereas Section 4 discusses the high-energy tail of cosmic rays interacting with molecular gas to produce γ-ray emission detected by *Fermi* and the H.E.S.S. telescopes.

2. NONTHERMAL RADIATION FROM DIFFUSE GAS

Nonthermal radio continuum emission is used to probe the population of cosmic-ray electrons. These cosmic-ray electrons may interact with the reservoir of molecular gas distributed in the Galactic center. An accurate measure of the cosmic-ray flux traced at radio wavelengths is critical to investigate the origin of γ-ray and X-ray emission in the context of bremsstrahlung emission. We first discuss radio measurements of the Galactic center to estimate the total nonthermal radio flux, followed by the analysis of γ-ray data from *Fermi*.

2.1. The Separation of Thermal and Nonthermal Radio Emission

The distribution of relativistic electrons is traced by synchrotron continuum emission at low radio frequencies. However, the large-scale study of radio continuum emission from the inner 200 pc of the Galaxy shows that the diffuse component is due to a mixture of thermal and nonthermal emission (e.g., Law et al. 2008). Thus, it is difficult to separate these two components spatially as their emission overlaps at radio wavelengths. Even more challenging is that some of the diffuse and extended sources have a spectral index, α, where the flux density $F_\nu \propto \nu^{-\alpha}$, that is flatter or harder than $\alpha = 0.5$ ($p = 2\alpha+1 = 2$ corresponding to energy spectrum E^{-p}). Apart from the large-scale diffuse nonthermal emission on a scale of several degrees (LaRosa et al. 2005; Crocker et al. 2010), there are several discrete sources of nonthermal emission. One is the population of nonthermal filamentary structures found throughout this region. These synchrotron filaments can be as long as $>15'$ (or 36 pc at the 8 kpc distance to the Galactic center) and narrow ($\approx 5''$–$10''$ corresponding to 0.2–0.4 pc). Polarization studies of the filaments trace an organized magnetic field which runs perpendicular to the Galactic plane (Yusef-Zadeh et al. 1984; Lang et al. 2002; Nord et al. 2004). Nonthermal emission also arises from supernova remnants in the Galactic center, some of which are interacting with molecular clouds, such as Sgr A East (SNR G0.0−0.0; e.g., Tsuboi et al. 2011). Another source of nonthermal emission is the population of pulsars that could contribute to nonthermal emission from this region (Johnston et al. 2006; Deneva et al. 2009; Wharton et al. 2012). Lastly, populations of compact stellar sources could produce nonthermal radiation from colliding winds in massive binary systems; two such examples have been detected in the Arches cluster and Sgr B2 (Yusef-Zadeh et al. 2003, 2007b).

A quantitative estimate of the relative amount of thermal and nonthermal emission from the Galactic center was made by Law et al. (2008) based on radio continuum data at 5 and 8.5 GHz taken with the GBT over the region between $357°.5 < l < 1°.2$ and $-0°.6 < b < 0°.4$. These authors assumed that thermal and nonthermal sources are separated from each other and identified them from the spectral index α values measured between 5 and 8 GHz. It was concluded that 85% and 76% of continuum radio flux from individual sources is due to nonthermal processes at 5 and 8 GHz, respectively. Earlier studies claimed that $\sim$50% of the continuum emission at 5 GHz is due to nonthermal emission (Schmidt 1980; Mezger & Pauls 1979). The discrepancy in the ratio of nonthermal to thermal emission could be due to the flat spectrum of some of the nonthermal sources, thus complicating the identification of thermal and nonthermal sources. LaRosa et al. (2005) studied diffuse radio continuum emission from the inner $6° \times 2°$ of the Galactic center at 75 and 327 MHz. They found a strong diffuse nonthermal structure with integrated flux density of 7000 Jy at 330 MHz. The spectral index value between 330 and 74 MHz gave $\alpha > 0.7$ which is a lower limit due to thermal absorption at 74 MHz. In another study, Crocker et al. (2010) investigated the spectrum of nonthermal emission from the inner $3° \times 2°$ and found a spectral break of 0.6 at 1.7 GHz.

To measure the distribution of radio flux from the inner $2° \times 1°$ of the Galactic center region, we integrated the total continuum flux at 0.325, 1.40, 8.5, and 5 GHz based on GBT observations described by Law et al. (2008) who focused only on 8.5 and 5 GHz data. A region away from the Galactic plane was selected having minimum contamination by Galactic center sources. To construct a background-subtracted image, a noise map was first constructed from the region that has been mapped by GBT. The noise map and a DC offset were then subtracted from the entire image. Figure 1(a) shows a continuum-subtracted image at 1.415 GHz from the inner $\sim$5° × 5° of the Galactic center. Prominent radio continuum sources along the Galactic equator such as Sgr A near $l \sim 0°$, radio continuum Arc near $l \sim 0°.2$, Sgr B near $l \sim 0°.7$, Sgr C near $l \sim -0°.6$, Sgr D near $l \sim 1°.2$, and the bright nonthermal source the Tornado nebula near $l \sim -2°.5$ show peaks in contours of 1.415 GHz emission (Yusef-Zadeh et al. 2004). The gray-scale image in Figure 1(b) shows weak extended structures distributed away from the Galactic ridge. Extended features distributed at positive latitudes are known as Galactic center radio lobes (e.g., Law et al. 2008). There are also large-scale features at negative latitudes near $l = -0°.9$ extending to $b \sim -1°$ associated with two supernova remnants G359.1−0.5 and G359.0−0.9 (Reich 1982; Reich & Reich 1986). A new feature, G359.02+0.27, is a long vertical structure running perpendicular to the plane extending toward more negative latitudes near $b \sim -1°.6$ between $l \sim -0°.075$ and $l \sim 0°.27$.
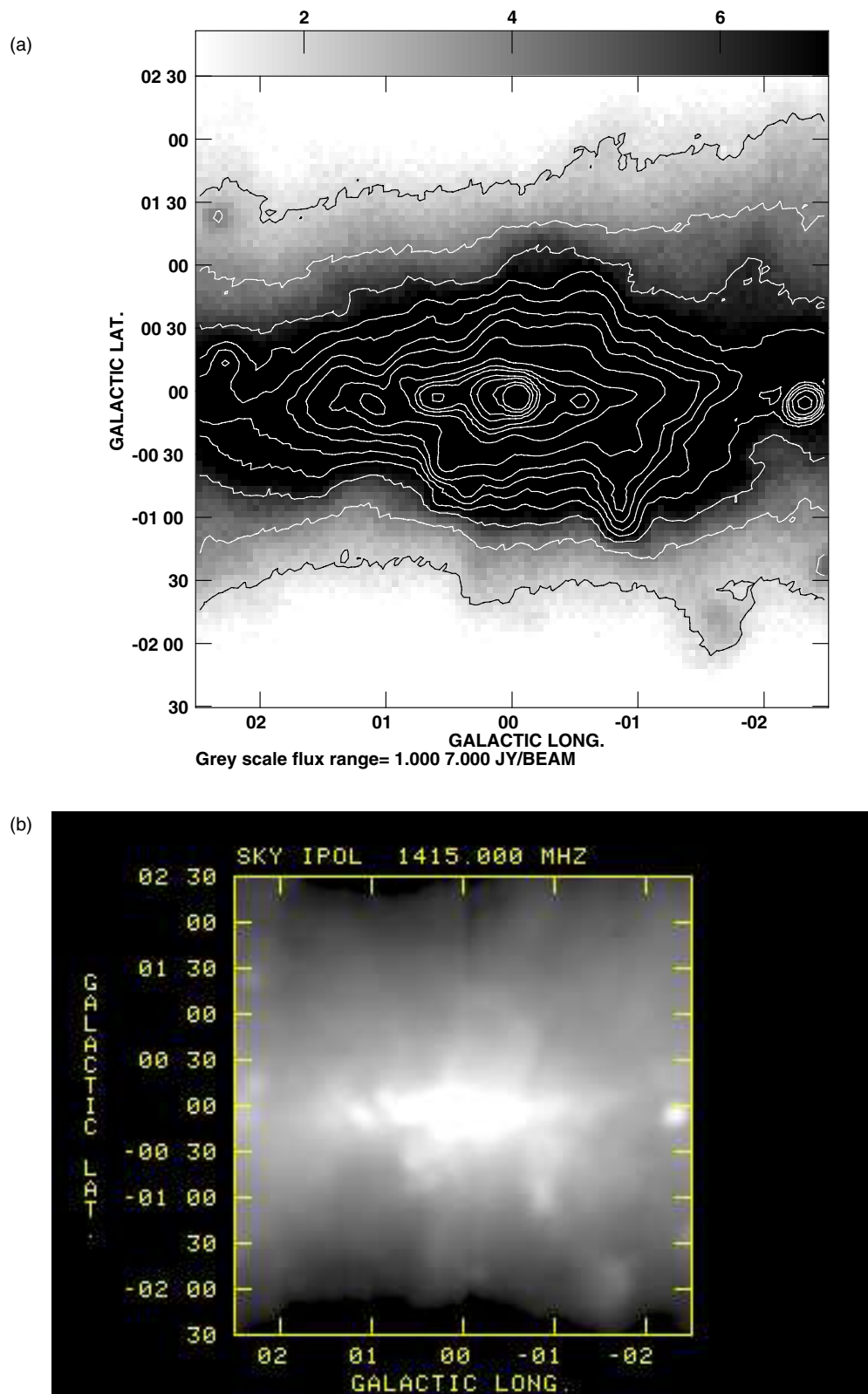
Figure 1. (a) Contours of background-subtracted continuum emission at 2, 4, 6, 8, 10, 12.5, 15, 20, 30, 40, 50, 75, 100, 150, and 200 Jy beam^{-1} are superimposed on a gray-scale image at 1.415 GHz with a spatial resolution of 539″. The gray scale ranges between 1 and 7 Jy beam^{-1}. (b) The same as (a) except that only the gray-scale image is shown. The prominent vertical features toward negative latitudes, $b \sim -2°$, are best displayed in this image.

(A color version of this figure is available in the online journal.)

Table 1
Integrated Radio Flux from the Inner $2° \times 0°.85$

Frequency (Hz)	Flux$\pm\sigma$ (Jy)	DC Offset (Jy)	rms Noise (Jy beam^{-1})
3.25×10^8	$3.57 \times 10^3 \pm 10.1$	127	5.8
1.41×10^9	$2.77 \times 10^3 \pm 1.1$	8.1	1.3×10^{-1}
4.85×10^9	$1.35 \times 10^3 \pm 0.6$	1.44×10^{-2}	2×10^{-2}
8.5×10^9	$7.11 \times 10^2 \pm 0.8$	1.2×10^{-2}	1.5×10^{-2}

We measured the flux from the brightest region of the maps at four different frequencies all based on GBT observations and presented the flux in Table 1. The first two columns of this table show the frequency and integrated flux from the inner $2° \times 0°.85$ of the Galactic center. The DC offset and the rms noise per beam, measured from blank regions of individual images of the survey, are listed in the last two columns, respectively. To illustrate the distribution of flux as a function of radius from the Galactic center, we made azimuthally averaged radial profiles of radio emission at all four frequencies, as shown in Figures 2(a)–(d). We used MIRIAD task `ellint` to integrate elliptical annuli with an aspect ratio of two centered on Sgr A*. The width of each annulus is one pixel corresponding to $20''$, $30''$, $30''$, and $600''$ at 8.5, 4.85, 1.415, and 0.325 GHz, respectively. The rms in Jy beam^{-1} was calculated and then scaled by the square root of the number of beams in each annulus. These plots show considerable flux variations as a function of frequency, suggesting that thermal and nonthermal features dominate the total observed flux at high and low frequencies, respectively.

To estimate the contribution of thermal and nonthermal emission, we use the integrated flux to derive spectral index values $\alpha_{1.4\,\mathrm{GHz}}^{325\,\mathrm{MHz}} = 0.17 \pm 0.01$, $\alpha_{4.5\,\mathrm{GHz}}^{1.4\,\mathrm{GHz}} = 0.58 \pm 0.01$, and $\alpha_{8.5\,\mathrm{GHz}}^{4.5\,\mathrm{GHz}} = 1.14 \pm 0.01$. The spectral index distribution is relatively flat at low frequencies whereas it becomes steeper at high frequencies. The variation of the spectral index is consistent with thermal emission from H II regions ($F_\nu \propto \nu^{-0.1}$) which becomes optically thick ($F_\nu \propto \nu^2$) at low frequencies. The flattening of the spectral index between 325 MHz and 1.415 GHz could result from the decrease of thermal flux due to free–free absorption of thermal gas that becomes opaque at low frequencies.

The true percentage of thermal and nonthermal emission from the complex region of the inner $2° \times 0°.85$ is very difficult to measure directly. In order to separate the intrinsic flux of thermal and nonthermal emission, we assumed that the two components are spatially mixed with or separate from each other following Gregory & Seaquist (1974). In this case, the observed flux in this model is given by

$$S_\nu = \Omega\,(S_{\mathrm{NT}}\exp(-\tau_\nu) + B_\nu(T)) \times (1 - \exp(-\tau_\nu)),$$

where $S_{\mathrm{NT}} \propto \nu^{-\alpha}$ is the nonthermal flux in the absence of free–free absorption, τ_ν is the free–free optical depth at frequency ν, $B_\nu(T)$ is Planck's function at the temperature T, and Ω is the solid angle subtended by the source. These calculations account for the spectral turnover at low frequencies due to opacity of diffuse thermal emission. Figure 3 shows the flux from the inner $2° \times 0°.85$ as a function of frequency. The solid black curve represents the χ^2-fit to the total flux which is itself decomposed into thermal and nonthermal components, shown as long- and short-dashed lines, respectively. We fix the thermal contribution at 4.85 GHz to be 25% (Law et al. 2008) and assume a kinetic temperature of 5000 K. We adopt a broken power law for the unabsorbed nonthermal emission and assume

that this component lies behind the thermal emission. With this model we find $\nu^{-0.25}$ below 3.3 GHz and $\nu^{-1.7}$ above 3.3 GHz, with an unabsorbed nonthermal flux of 2450 Jy at 325 MHz. Because the optical depth is only significant below 200 MHz, there is no difference between assuming that the thermal and nonthermal components are mixed in versus having the thermal emission be a foreground screen. Using a 25% contribution from thermal emission at 8.5 GHz (Law et al. 2008) corresponds to an emission measure $EM \sim 10^4$ cm^{-6} pc. This gives an average electron density $n_e \sim 6$ cm^{-3} assuming that it is uniformly distributed over $L \sim 288$ pc.

The study of the cosmic rays in the Galactic disk has recently suggested a need for a low-energy break in the spectrum of cosmic-ray electrons (Strong et al. 2011). This is not dissimilar to the spectral break that we infer from the cosmic-ray electrons in the Galactic center. An unusual aspect of the spectrum of radio emission from the Galactic center is the large change in particle distribution index $\sim$1.7. The energy spectrum of electrons corresponding to a broken power law is hard corresponding to $p = 1.5$ at low energies whereas the spectrum is steep at high energies with $p = 3.2$. A non-standard possibility that can account for such a large change in the spectral index value is the contribution of electrons and positrons produced as the byproduct of dark matter annihilation. In this picture, the electrons and positrons created through the annihilation of a relatively light ($\sim$5–10 GeV) dark matter particle can provide a new population of electrons at energies less than the annihilation energy of WIMPS. Although this picture is by no means unique in explaining the large change in the spectral index, spectral distribution of electrons and positrons which emit synchrotron radiation is consistent with the observed spectral shape of electrons for individual nonthermal radio filaments at high frequencies (Linden et al. 2011).

2.2. Gamma-ray Emission from the Galactic Center

Extended γ-ray emission within the inner $2°$ has been detected at TeV energies by the H.E.S.S. atmospheric Cherenkov telescope. The Galactic center ridge of γ-ray emission (hereafter, Galactic ridge) appears well correlated with the molecular gas distribution in the inner region (Aharonian et al. 2006).

The Galactic center is also a prominent sources of GeV γ-rays. The *Compton Gamma Ray Observatory* identified a source coincident with the Galactic center, 2EG J1746–2852, at energies of 0.2–10 GeV (Thompson et al. 1995). With greatly improved sensitivity and spatial resolution, the *Fermi* LAT resolves multiple GeV sources in the inner $2°$ of the Galaxy. A bright point source coincident with the position of Sgr A is reported in the LAT First and Second Source Catalogs (Abdo et al. 2010a; Nolan et al. 2012, hereafter 1FGL and 2FGL). Emission from the central source, 2FGL J1745.6–2858, shows a peak at a few GeV.

Several explanations have been proposed for the GeV emission in the Galactic center detected by *Fermi*. Chernyakova et al. (2012) propose that this central γ-ray source is produced by the diffusion of cosmic-ray protons into the surrounding dense molecular gas in the inner 10 pc. A separate analysis by Hooper & Goodenough (2011) claims the existence of a diffuse γ-ray source in the inner degree of the Galactic center, on top the Galactic diffuse background. This emission peaks at 2–4 GeV, which they interpret as the possible annihilation of dark matter. Alternatively, this feature could arise from a population of millisecond pulsars in the region (Abazajian 2011) or may be due
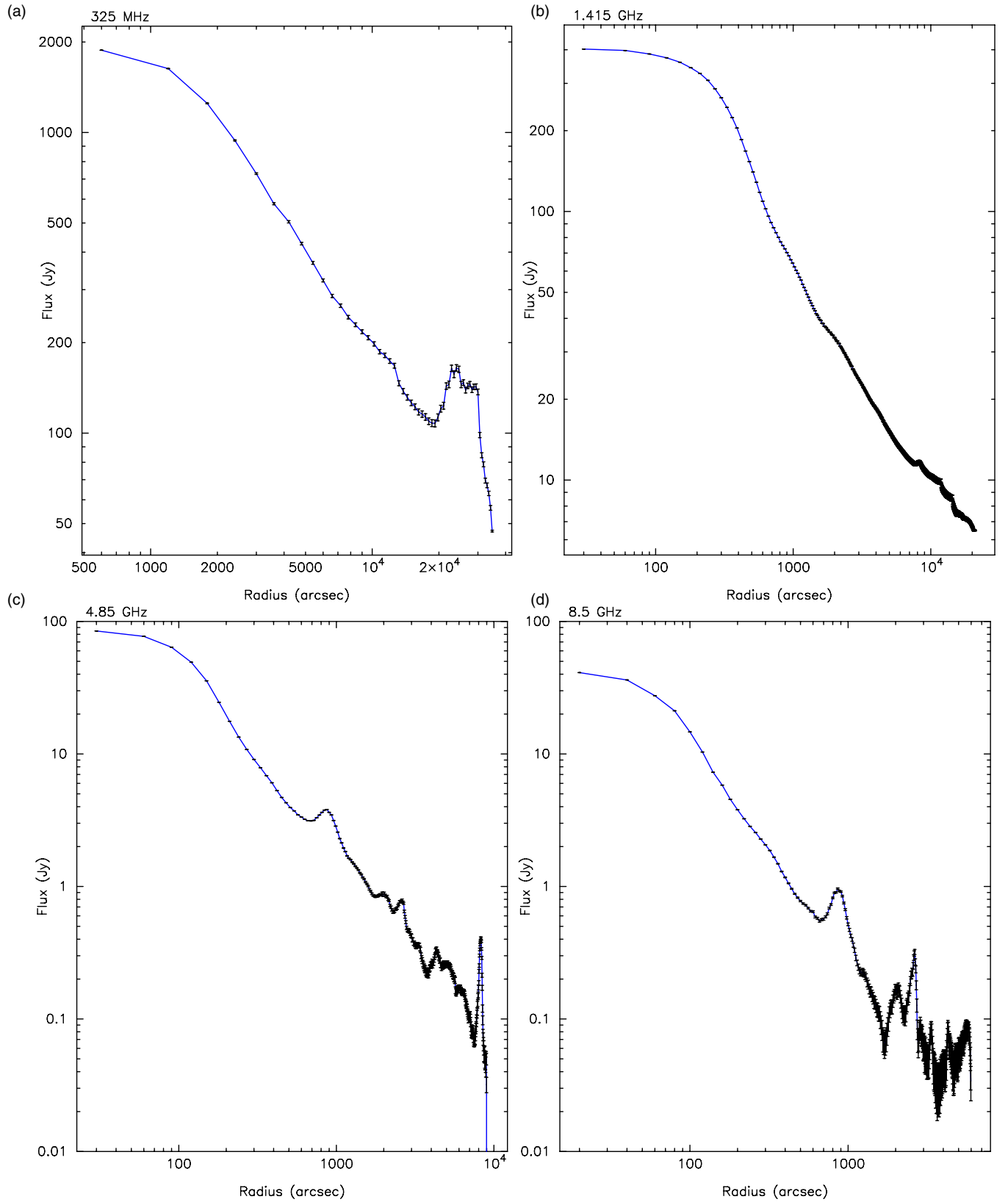
Figure 2. Distribution of flux as a function of radius from the Galactic center is made by azimuthally averaging radial profiles of radio emission at 325 MHz, 1.415 GHz, 4.85 GHz, and 8.5 GHz with spatial resolutions of 2328″, 539″, 153″, and 88″ and are shown in (a)–(d), respectively. The error bars of azimuthally averaged flux are also superimposed. The plots and the errors are logarithmic.

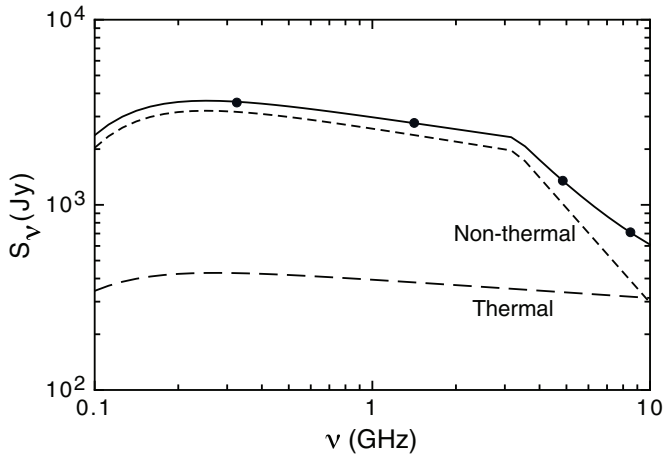(A color version of this figure is available in the online journal.)

Figure 3. Plot of the decomposition of the diffuse radio flux from the Galactic center into thermal and nonthermal components. We fixed the thermal contribution at 4.85 GHz to be 25% of the total flux and assumed a kinetic temperature of 5000 K. We used a broken power law for the unabsorbed nonthermal emission which is considered to lie behind the thermal screen. The black dots represent the observed flux at a given frequency.

to improperly accounting for known point sources in the region (Boyarsky et al. 2011).

Interestingly, the hard spectrum of the filaments of the Arc that emit radio synchrotron radiation could be a strong source of cosmic rays responsible for the excess γ-ray emission within the inner $30'$ of the Galactic center (Linden et al. 2011). The Galactic center nonthermal filaments of the radio Arc are unique in the Galaxy and have a harder spectrum compared to typical nonthermal radio sources. We will argue in Section 4 that the interaction of relativistic electrons with molecular gas in the Galactic center produces significant bremsstrahlung radiation, and that the distribution of diffuse γ-ray emission correlates well with the distribution of both nonthermal radio continuum emission and the 6.4 keV Kα line emission. Here, we analyze the γ-ray emission from the Galactic center using three years of *Fermi* LAT data, in order to characterize emission from both the central γ-ray source, as well as nonthermal emission from the Galactic ridge.

2.2.1. Fermi LAT Observations

Fermi LAT detects γ-rays between $\sim$20 MeV and $>$300 GeV in an all-sky scanning mode, observing the entire sky every $\sim$3 hr (Atwood et al. 2009). Events are detected by the LAT tracker in both the "front" and "back" sections, which are combined in this analysis. Events were selected within a radius of interest of $30°$ from the Galactic center, and for times between 2008 August 4 and 2011 August 4, and at energies between 1 GeV and 100 GeV. The angular resolution (68% containment angle for events at incident angle) is $\sim$0°9 at 1 GeV, increasing to 0°2 at the highest energies. The point-spread function (PSF) is detailed on the Fermi Science Support Center (FSSC) Web page.[8] The energy resolution of the LAT is 8%–10% between 100 MeV and 100 GeV. The systematic uncertainties in the IRF are energy dependent: 8% at 100 MeV, 5% at 560 MeV, and 10% at 10 GeV.[9]

Data are analyzed using the *Fermi* Science Tools (v9r15p2) with the "P7SOURCE_V6" instrument response functions.

Only source class events with Earth zenith angles less than $100°$ have been used to reduce contamination from the Earth limb. We use the standard maximum likelihood fitting, with photons binned in 0°05 pixels within a $10° \times 10°$ region centered on Sgr A. Data are also binned spectrally with four log-normal bins per decade in energy between 1 and 100 GeV. We restrict our analysis only to these high energies at which the PSF of the LAT is sufficient to spatially resolve sources within the central $2° \times 1°$ region.

For source modeling, we include all sources in the 2FGL source catalog (Nolan et al. 2012). Additionally, we include the standard isotropic model which accounts for the extragalactic diffuse background and residual instrumental background ("iso_p7v6source.txt") and Galactic diffuse model which accounts for interactions between cosmic rays and the Galactic interstellar medium (ISM) and photon field ("gal_2yearp7v6_v0.fits"). The Galactic diffuse model[10] is derived from a fit to two years of LAT data using Galactocentric rings derived from tracers of the interstellar gas distribution (H I and CO) and a model of inverse Compton emission calculated using GALPROP (Strong et al. 2004).

To estimate the systematic uncertainty from the diffuse model, we change the best-fit normalization of the diffuse components by $\pm$6%, following the method used for analysis of unresolved or small-scale sources, such as Galactic supernova remnants (Abdo et al. 2010b). This value was determined by using different versions of the Galactic diffuse emission generated by GALPROP (Strong et al. 2004) to compare the γ-ray intensity of nearby source-free regions of the Galactic plane with that expected from the models (Abdo et al. 2010b). We note that the use of the Galactic diffuse model is only appropriate for analysis of small diameter sources and has been employed for other extended GeV sources as large as a few degrees in extension.

An additional source of uncertainty arises as we must assume a morphology for GeV emission from the inner $\sim$2° of the Galaxy in our likelihood fit. Figure 4(a) shows a smoothed counts map at $\geqslant$1 GeV, after subtraction of the isotropic and Galactic diffuse templates. Prominent emission is seen from the vicinity of Sgr A, with fainter emission extending along the Galactic plane. Additionally, there are point sources that lie off the plane of the Galaxy, and a faint complex of emission coincident with TeV source H.E.S.S. J1745−303. For comparison with the distribution of nonthermal emission from the same region, Figure 4(b) shows the positions of 2FGL sources superimposed on 20 cm radio continuum emission observed by the GBT. Ellipses indicate the 68% error in the source localization. These sources are listed in Table 2 and are described in the following section. The 2FGL catalog decomposes emission above the Galactic diffuse model as individual point sources, however, we also test the hypothesis that the emission arises from an extended component along the Galactic ridge.

To obtain the best possible model of the emission, we relocalize the positions of all 2FGL point sources in the inner 2° and refit their spectra using only $>$1 GeV data. We search for unmodeled point sources by creating test statistic maps of the residual emission. The test statistic is a measure of the significance of adding a source to a model, defined as TS $= 2 \log(\mathcal{L}_1/\mathcal{L}_0)$ where $\mathcal{L}$ is the Poisson likelihood, and the subscripts 0 and 1 refer to the original model and a model

---

[8] http://fermi.gsfc.nasa.gov/ssc/data/analysis/documentation/Cicerone/Cicerone_LAT_IRFs/IRF_PSF.html

[9] http://fermi.gsfc.nasa.gov/ssc/data/analysis/LAT_caveats.html

[10] Details are available at the FSSC: http://fermi.gsfc.nasa.gov/ssc/data/access/lat/Model_details/Pass7_galactic.html
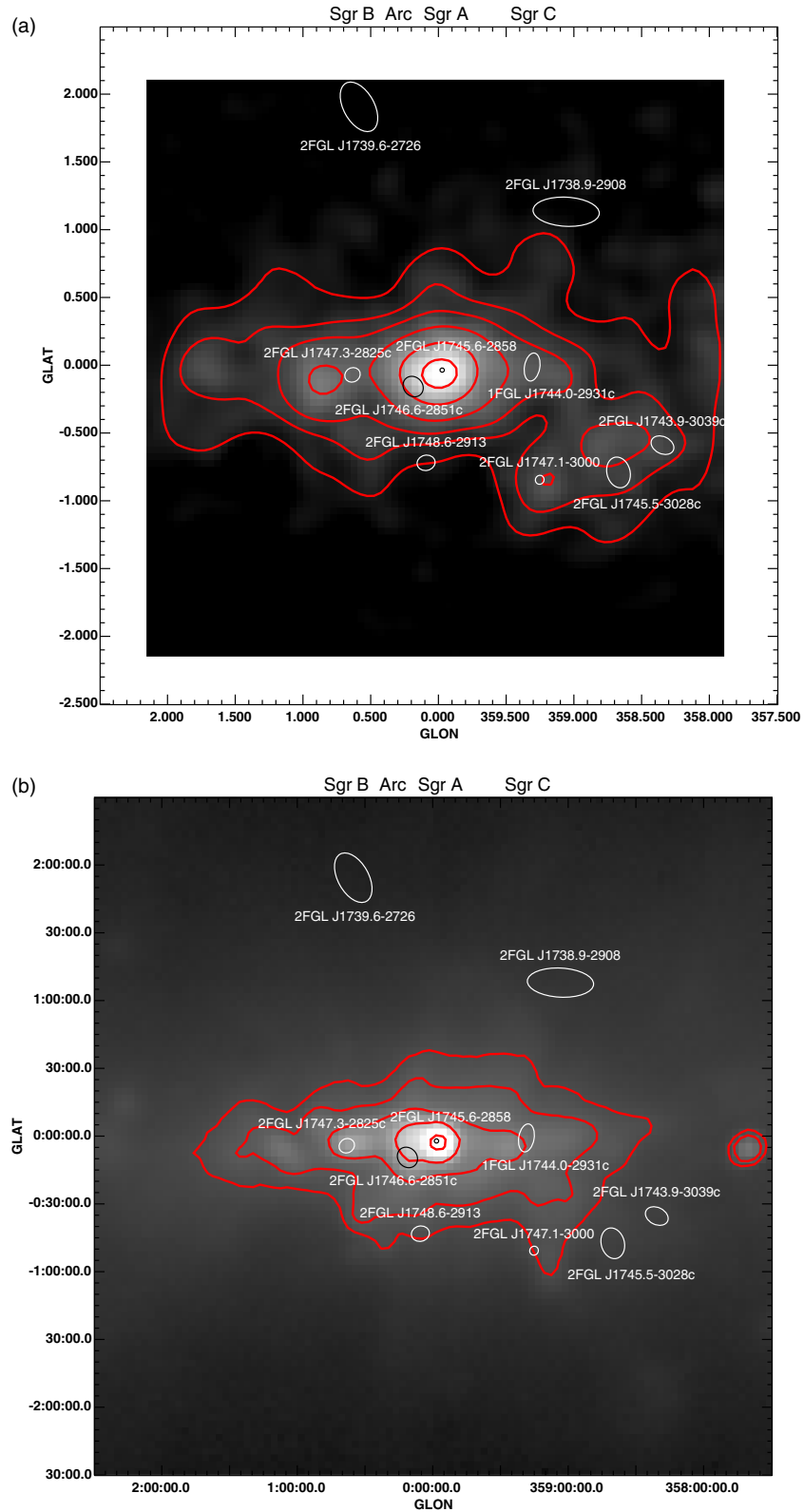
Figure 4. (a) Contours of *Fermi* LAT γ-rays between 1 and 300 GeV are superimposed on gray-scale background-subtracted image of *Fermi* LAT γ-rays between 1 and 300 GeV. The sources identified by the centroid 95 contour levels are set at 2000, 3600, 4800, 6400, 9000, and 13,000 counts deg^{-2}. (b) Similar to (a) except that contours of radio emission at 1.4 GHz based on GBT observations are superimposed on a gray-scale image at 1.4 GHz. The longitudes of Sgr A, Sgr B, Sgr C, and the radio Arc are labeled. Contour levels are set at 13, 20, 40, 100, 300 Jy beam^{-1}.

(A color version of this figure is available in the online journal.)

Table 2
Detected γ-ray Sources in the Inner $2°$ of the Galaxy

Name	R.A. (h m s)	Dec ($°$ $'$ $''$)	Flux (1–100 GeV) (10^{-9} photons cm^{-2} s^{-1})	TS	Association
2FGL J1745.6−2858	17 45 41.6	−28 58 43	77.3(2.0)	1857	Sgr A
2FGL J1746.6−2851c	17 46 40.6	−28 51 31	6.6(1.4)	35	the Arc
2FGL J1747.3−2825c	17 47 23.9	−28 25 53	14.2(1.4)	112	Sgr B
1FGL J1744.0−2931c	17 44 01.0	−29 31 57	10.0(1.4)	79	Sgr C
2FGL J1747.1−3000	17 47 09.2	−30 00 50	25.0(1.1)	729	PSR J1747−2958
2FGL J1745.5−3028c	17 45 32.4	−30 28 56	4.3(0.9)	26	H.E.S.S. J1745−303
2FGL J1743.9−3039c	17 43 57.3	−30 39 13	3.7(0.8)	25	H.E.S.S. J1745−303
2FGL J1748.6−2913	17 48 39.2	−29 13 53	12.0(1.0)	169	
2FGL J1738.9−2908	17 38 56.7	−29 08 25	6.8(0.8)	234	
2FGL J1754.1−2930	17 54 08.9	−29 30 33	3.6(0.5)	83	
bkgA	17 40 01.2	−28 31 59	3.6(0.7)	45	

with an additional source, respectively. Within $2°$ of the Galactic center, we find two significant sources with TS > 25 that are not listed in 2FGL. A source is found near the location of Sgr C, α, δ(J2000) = 266.044, −29.323, previously identified as 1FGL J1744.0−2931c. Another source is found $0°.5$ away from the Galactic ridge at positive latitudes, α, δ(J2000) = 265.005, −28.533, and has a very soft spectrum, $\Gamma = 2.9 \pm 0.2$, above 1 GeV. Adding these two additional sources improved the model of GeV emission, as shown in Table 2. We refer to this model as the "2FGL refit" model hereafter.

Sources are initially assumed to have a power-law spectrum. For highly significant sources we attempted to replace a simple power-law spectral model with a broken power-law model of the form

$$\frac{dN}{dE} = N_0 \times \begin{cases} (E/E_b)^{\Gamma_1} & \text{if } E < E_b \\ (E/E_b)^{\Gamma_2} & \text{if } E > E_b \end{cases}. \quad (1)$$

For Sgr A*, we find a broken power law improves the fit. The best-fit spectral parameters are $\Gamma_1 = 1.9$, $\Gamma_2 = 3.0$, and $E_b = 3$ GeV.

2.2.2. Point Sources in the Inner Galaxy

We briefly summarize point sources detected in the inner $2°$. Source 2FGL J1745.6−2858 corresponds to the position of Sgr A*. This source has been studied in detail by Chernyakova et al. (2012) and Linden et al. (2012). The *Fermi* LAT spectrum connects to that of the detected H.E.S.S. TeV source at $\sim$100 GeV, with a softening of the spectrum between 1 and 100 GeV, and a hardening of the spectrum at >100 GeV to multi-TeV energies. In addition to emission from Sgr A*, there are two point sources corresponding to the locations of the Arc and Sgr B (sources 2FGL J1746.6−2851c and J1747.3−2825c, respectively). Faint emission was reported in the vicinity of Sgr C in 1FGL, but the source was not present in 2FGL. We note these three point sources closest to the Galactic center (corresponding with the Arc, Sgr B, and Sgr C) appear coincident with the diffuse emission detected at TeV energies by H.E.S.S. We explore this further in the following section.

Other sources are also present within the inner $2°$ that are not thought to be associated with the Galactic center region. The Mouse pulsar corresponds to source 2FGL J1747.1−3000, with detected γ-ray pulsations. However, this pulsar is known to lie at a distance of only 5 kpc (Camilo et al. 2002). Two sources (2FGL J1743.9−3039c and J1745.5−3028c) appear to be counterparts to the extended TeV source H.E.S.S. J1745−303. These sources may be related to the SNR G359.1−0.5, known to be interacting

with molecular clouds, or may be candidate pulsar wind nebulae (Aharonian et al. 2008). In either case, these sources lie outside the Galactic ridge. There are also three sources detected more than half a degree off the Galactic plane, with no readily apparent counterparts (2FGL J1738.9−2908, J1748.6−2913, and J1754.1−2930). Similarly, the newly detected source "bkgA" also lies above the Galactic plane and has no apparent multi-wavelength counterpart. The off-plane GeV sources show no correlation with the diffuse background model, or large-scale structures seen toward the Galactic center, and are therefore unlikely to have any relation to the Galactic ridge.

2.2.3. Emission from the Galactic Ridge

To probe whether GeV emission is present on extended spatial scales, we replace the three point sources associated with the Arc, Sgr B, and Sgr C with an extended spatial template. We then maximize the likelihood using the extended spatial template plus a point source that accounts for emission from Sgr A. We separately apply four template models: 20 cm radio continuum, X-ray Fe I Kα line emission, H.E.S.S. diffuse TeV emission, and CS 1–0 integrated line intensity representing the distribution of dense gas in the region. All templates span roughly the inner $2° \times 1°$. In the 20 cm and H.E.S.S. templates, the central emission from Sgr A* is removed, as it is clearly detected as a point source with a unique spectrum. Fitting the spatial templates from other wavelengths gives a means of comparing them with the morphology of GeV emission from the Galactic ridge above the modeled Galactic diffuse.

First, we add an extended spatial template using the CS 1–0 map (Tsuboi et al. 1999). As CS is an optically thin tracer of dense gas, this model probes the distribution of dense clouds in the Galactic center region. However, we find that replacing the three point sources with the CS template results in a significantly lower global likelihood than the point source model. This is likely due to the fact that CS emission is detected at Galactic longitudes >$1°$ while TeV and GeV emission do not appear to extend this far from the Galactic center.

We do find an improved fit when the point sources in the Galactic ridge are replaced by other spatial templates representing the distribution of X-ray Fe I Kα line, H.E.S.S. TeV, and diffuse 20 cm radio emission. The X-ray data that we used are based on *Chandra* observations (Yusef-Zadeh et al. 2007a). Table 3 presents the six models which we fit to the LAT data. The 2FGL point source models have 12 degrees of freedom (Sgr A with a broken power law, three point sources with power-law spectra, and the isotropic and Galactic diffuse normalizations). The extended models require four fewer degrees of freedom

Table 3
Comparison of Spatial Template Fits to *Fermi* LAT Data $\geqslant$1 GeV

Model	$2 \log(\mathcal{L}_1/\mathcal{L}_0)$	dof
2FGL	0	12
2FGL refit	51	12
X-ray Fe Kα	68	8
H.E.S.S. residual	101	8
20 cm radio	113	8
CS gas	−103	8

since the three point sources are replaced by one source. We note that the TeV and radio templates provide a better fit to the data than the X-ray line template, though this may be due to non-uniform sensitivity of the X-ray observations.

We conclude that the GeV emission from the Galactic ridge is well correlated with the extended morphologies observed at radio, TeV, and X-ray wavelengths. We note that the Galactic ridge emission has sufficient statistics to fit with a broken power-law spectral model. Using the TeV template, we find that the best-fit spectral parameters are $\Gamma_1 = 1.8$, $\Gamma_2 = 3.0$, and $E_b = 2.5$ GeV. However, we caution that despite the improvement in the likelihood, the spatial template and point source models are not nested, so a significance of the improvement of the extended templates over the point source model cannot be stated. We also note that while simply increasing or decreasing the normalization of the diffuse Galactic model cannot fit the emission observed by the LAT in the Galactic ridge, we have not performed an in-depth study of the diffuse emission for the Galaxy. However, that the GeV emission is consistent with the morphology of extended nonthermal emission observed at other wavelengths is suggestive of a common origin. We discuss in detail a plausible model for nonthermal emission from the Galactic ridge in Section 4.

2.3. X-Ray Emission from the Galactic Center

2.3.1. Chandra Data

The results of large-scale *Chandra* observations of the Galactic center focusing on the distribution of Fe I Kα line emission were described in Yusef-Zadeh et al. (2007a). Since the publication of these results in 2007, additional *Chandra* observations of this region have been carried out. Here, we use 15 additional pointings with exposure time of 40 ks each. These new observations are combined with additional archived data sets described in detail by Muno et al. (2009) who presented a catalog of X-ray sources in the inner $2° \times 0°.8$ of the Galactic center. We reproduce below the description of data reductions that were given for earlier analysis of 6.4 keV line emission (Yusef-Zadeh et al. 2007a).

Images of the equivalent widths (EWs) of the low-ionization 6.4 keV line of Fe I Kα were constructed using the techniques described by Park et al. (2004). Adaptively smoothed images of the diffuse line emission were generated in the same manner as the continuum image, using the 6.25–6.50 keV band for Fe I Kα. The continuum under each line was computed based on adaptively smoothed images of the flux in the 5.0–6.1 keV and 7.15–7.30 keV energy bands. We assumed that the flux in each continuum band (F_{band}) could be described as a power law, so that the normalization (N) and slope (Γ) of the power law could be computed from

$$F_{\text{band}} = \frac{N E_{\text{low}}^{-\Gamma+1} - N E_{\text{high}}^{-\Gamma+1}}{\Gamma - 1}. \quad (2)$$

Using the fluxes in both continuum bands, the above equation was solved for N and Γ using Newton's algorithm and the parameters were used to estimate the continuum contribution to the line emission images. To derive the EW images, we subtracted the estimated total continuum flux from the line image, and then divided the line image by the continuum flux density at the centroid of the line (6.4 keV). We caution that we have neglected the cosmic-ray background in generating these maps, which could account for as much as ∼40% of the events in the 6–7 keV band and consequently biases any estimate of the EW. The assumption of a power-law spectrum instead of multiple plasma temperatures especially corresponding to the He-like Kα line at 6.7 keV also introduces a small systematic bias in these maps. From Figure 5 in Muno et al. (2004), the nonthermal X-ray flux is estimated to be about one-third of the continuum flux at the Fe I Kα line band. We have not attempted to correct these effects because they are only used to search for regions of enhanced iron emission. In order to confirm the properties suggested by *Chandra* images of the diffuse line and continuum emission, we compared the *Chandra* EW map with that constructed from *Suzaku* measurements.

2.3.2. Suzaku Data

To check the accuracy of the EW map measured from *Chandra* observations, we derived the distribution of Fe I Kα line emission and EW map using the *Suzaku* data. The details of the *Suzaku* observations are shown in Table 1 of Uchiyama et al. (2011), which partially covers the region between $−3° < l < 2°$ and $−1° < b < 1°$.

We made X-ray images in the energy bands of 5–6 and 7–8 keV for continuum emissions and 6.3–6.5 keV for Fe I Kα. We sorted non X-ray background (NXB) data by the cutoff rigidity with `xisnxbegen` (Tawa et al. 2008) and made NXB images in the foregoing energy ranges for the respective observations. The NXB images are subtracted from the X-ray images. Thus, in the case of the *Suzaku* image, the effects of the NXB are removed with an uncertainty of less than ∼4% (Tawa et al. 2008). After the NXB subtraction, the vignetting effects of the X-ray images are corrected with `xissim` (Ishisaki et al. 2007). Both `xisnxbegen` and `xissim` are included in the HEASoft package.[11] We calculated the continuum flux in the 6.3–6.5 keV band from the 5–6 and 7–8 keV band images, following a similar technique that was applied to *Chandra* data. We subtracted the calculated continuum image from the 6.3–6.5 keV band image and obtained the Fe I Kα line emission map. The Fe I Kα line emission map was divided by the continuum image before the EW map was constructed. Bright point sources, 2E 1743.1−2842, 2E 1742.9−2929, and 2E 1740.7−2943 are masked by circles with a radius of $3°.5$. We ignored the cosmic X-ray background (CXB) when we made the EW map. It is because that the interstellar absorption of the CXB is difficult to estimate. Assuming the CXB flux of Kushino et al. (2002), the systematic errors of the EW in Figure 9 are estimated to be less than 20%.

3. EVIDENCE FOR COSMIC-RAY INTERACTIONS

To examine the bremsstrahlung model of cosmic-ray electrons interacting with molecular gas, we studied several consequences of such an interaction to provide a self-consistent check on the applicability of this model. In the following sections we

---
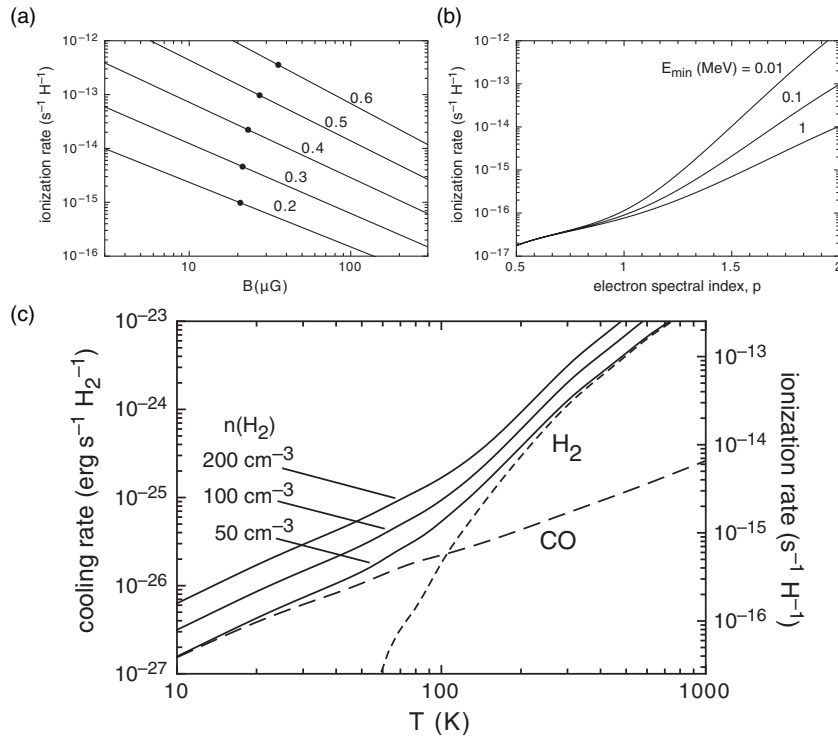
[11] http://heasarc.nasa.gov/lheasoft/

Figure 5. (a) The variation of cosmic-ray ionization rate as a function of the magnetic field for different values of the spectral index of the radiation α. The black dot on each curve gives the value at which the magnetic field and particle energies are in equipartition. (b) This plot shows how the ionization rate inferred from the nonthermal diffuse Galactic center flux at 325 MHz depends on electron energy spectral index p and the lower energy cutoff $E_{\min}$. (c) Solid curves show the total cooling rate for diffuse molecular gas for H_2 densities of 50, 100, and 200 cm^{-3}. Only the dominant cooling, by rotational transitions of H_2 and CO, has been included; these contributions for $n(H_2) = 50$ cm^{-3} are indicated by the short-dashed and long-dashed curves, respectively. A gas-phase abundance of $CO/H_2 = 2.8 \times 10^{-4}$ has been adopted, appropriate for a metallicity twice that of the Sun. The right-hand axis shows the ionization rate by cosmic-ray electrons needed to supply the corresponding heating rate, assuming that each ionization is associated with the deposition of 12.4 eV of heat (see the text).

show the feasibility of cosmic-ray electrons interacting with molecular gas to explain the unique characteristics of molecular gas in the Galactic center region as well as production of γ-ray and X-ray emission.

3.1. Cosmic-ray Ionization Rate and the Magnetic Field Strength

Cosmic rays play an important role in star formation processes as they are a primary source of ionization of dense molecular clouds: driving ion–neutral chemistry, heating the gas, and determining the coupling to magnetic fields. Recent measurements indicate a vast amount of diffuse H_3^+ and H_3O^+ distributed in the Galactic center. This suggests a cosmic-ray ionization rate $\zeta \sim 10^{-15}$ s^{-1} H^{-1}, one to two orders of magnitude higher in the Galactic center region than in the Galactic disk (Oka et al. 2005; van der Tak et al. 2006).

Here we consider whether this high ionization rate may be produced by the low-energy tail of the population of relativistic cosmic-ray electrons that are responsible for the observed synchrotron emission in the Galactic center. We use the observed synchrotron flux to estimate their contribution to the cosmic-ray ionization rate, independent of H_3^+ measurements.

Unfortunately, the synchrotron intensity also depends not just on the cosmic-ray electron population but also on the magnetic field strength, which is quite uncertain. Early estimates inferred a large-scale milligauss magnetic field permeating throughout the Galactic center based on the apparent resistance of nonthermal filaments to distortion by molecular clouds (Yusef-Zadeh et al. 1984; Morris & Serabyn 1996; Morris 2007). More recent estimates are somewhat lower: 6 μG was inferred from radio emission distributed over the inner 6° × 2° (LaRosa et al.

2005), whereas Crocker et al. (2010) inferred a minimum value $B \sim 50$ μG based on the nonthermal radio emission from the inner 3° × 2° of the Galaxy. In the face of these uncertainties, we adopt a fiducial value of 100 μG and consider the scaling with magnetic field in our results.

The cosmic-ray ionization rate per hydrogen nucleus, ζ, is directly proportional to the number density of cosmic-ray electrons (and also depends on their energy spectrum). The value of ζ is dominated by the number of low-energy electrons, and so is sensitive to the choice of lower energy electron cutoff. We adopt an E^{-p} electron spectrum running between $E_{\min} = 0.1$ MeV and $E_{\max} = 10$ GeV, a magnetic field B, and a line-of-sight depth L of the source region, which enable us to calculate both the synchrotron intensity I_ν at frequency ν and the ionization rate ζ in the source region. This yields the relationship

$$\zeta \approx \frac{3.1 \times 10^{-14}}{p-1} \frac{I_\nu}{\text{Jy arcmin}^{-2}} \left(\frac{\nu}{\text{GHz}}\right)^\alpha \left(\frac{L}{30\,\text{pc}}\right)^{-1}$$
$$\times \left(\frac{B}{100\,\mu\text{G}}\right)^{-(1+\alpha)} \text{s}^{-1}\,\text{H}^{-1}, \tag{3}$$

where $\alpha = (p-1)/2$ is the synchrotron spectral index and $I_\nu \propto \nu^{-\alpha}$ (so the product $I_\nu \nu^\alpha$ in this expression is constant). We estimate a total nonthermal flux at $\nu = 325$ MHz of 2.45×10^3 Jy arising from the inner 2° × 0°.85 ($L \sim 288$ pc) of the Galaxy. This emission is patchy, and so is assumed to fill 10% of the volume of an oblate spheroid with principal axes 2° × 2° × 0°.85.

Figures 5(a) and (b) illustrate the dependence of the inferred ionization rate on the spectral index, magnetic field strength,

and the lower energy cutoff of the electron spectrum. Figure 5(a) shows the ionization rate as a function of magnetic field strength for α running between 0.2 and 0.6. The ionization rate decreases with increasing field strength because fewer electrons are required to yield the same synchrotron emissivity. The black dot on each curve gives the equipartition magnetic field; this should be a lower limit on B, and so indicates the maximum ionization rate expected for each value of α. The ionization rate increases for steeper spectra and a fixed emissivity at the observed frequency, as there is a successively larger population of lower-energy electrons radiating at lower frequencies. Figure 5(b) illustrates the dependence of the ionization rate on these lower-energy electrons by varying the electron spectral index p and the lower energy cutoff $E_{\min}$ assuming an equipartition field. The dependence is weak for flat spectra ($p \lesssim 1$) but becomes marked for steep spectra.

For the observed range of spectral indices, $\alpha \sim 0.2$–0.3 and the equipartition magnetic field is $\sim$20 μG. The implied ionization rate is $\sim 10^{-15}$–10^{-14} s^{-1} H^{-1}. This is consistent with H$_3^+$ measurements toward several clouds in the Galactic center (Oka et al. 2005; Goto et al. 2008) which imply values of $\zeta \sim 2$–7×10^{-15} s^{-1} H^{-1} and a large reservoir of warm and diffuse ionized molecular gas (H$_3^+$) in the central region of the Galaxy. A strong milligauss field permeating the central regions of the Galaxy would imply $\zeta \sim 10^{-18}$ s^{-1} H^{-1}, much lower than that inferred from H$_3^+$ measurements. Our estimate of the magnetic field is also consistent with that of LaRosa et al. (2005) who inferred a field strength of 6 μG over the inner 6$^\circ \times$ 2° of the Galaxy.

Our estimated equipartition magnetic field strengths neglect the possible contribution of comic-ray protons to the particle energy density. The presence of a significant proton component increases the equipartition field strength, beyond the values indicated by black dots in Figure 5(a), by a factor of 2–4 for proton energy density 10–100 times that for the electrons, decreasing the cosmic-ray electron density needed to explain the observed synchrotron emission and hence decreasing the ionization rate by similar factors. The field strength would then be closer to the estimate made by Crocker et al. (2010).

3.2. Molecular Gas Heating Rate

Another consequence of the interaction of cosmic-ray electrons with molecular clouds is heating of molecular gas. This heating process is particularly relevant to the population of molecular clouds showing two different gas temperatures (Güsten et al. 1981; Mauersberger & Henkel 1993; see the review by Ferriere 2009 and references therein). A high spatial resolution study observed 36 clouds distributed between $l = -1^\circ$ and 3° using six transitions of NH$_3$ (Hüttemeister et al. 1993). These observations found a two-temperature distribution of molecular clouds, with the warm ($T_{\text{kin}} \sim$200 K) gas at low H$_2$ density of $n \sim 10^3$ cm^{-3} and cool ($T_{\text{kin}} \sim$25 K) gas to dense cores with $n \sim 10^5$ cm^{-3}. In another study, *Infrared Space Observatory* observations of rotational transitions of H$_2$ found predominantly warm molecular gas with $T \sim$ 150 K toward 16 Galactic center molecular clouds with H$_2$ column densities of $\sim$1–2 $\times 10^{22}$ cm^{-2} (Rodriguez-Fernández et al. 2001). The high gas temperature of the Galactic center molecular clouds is elevated from 30–50 K up to $T \sim$ 200 K (Lis et al. 2001) and is discrepant with respect to the dust temperature 18–22 K measured from observations of the inner 2$^\circ \times$ 1° of the Galaxy (Pierce-Price et al. 2000; Monlinari et al. 2011). The cause of high temperature molecular gas may be due to shocks generated as a result of cloud–cloud collisions (Rodriguez-Fernández et al.

2001). However, this mechanism is expected to produce warm gas only at the surface of the clouds where clouds collide with each other. Comic rays, on the other hand, have the advantage that they can increase the temperature throughout the cloud, even the heavily shielded dense regions.

Although on average one ion–electron pair is produced for every 40.1 eV lost by a cosmic-ray electron (Dalgarno et al. 1999), the heating associated with cosmic-ray electron ionization occurs because 11% of the 40.1 eV cosmic-ray energy loss associated with each ionization of a hydrogen molecule is consumed as heat (e.g., Dalgarno et al. 1999). Another 8 eV appears as heat when H$_3^+$ recombines (e.g., Maloney et al. 1996). Thus, each ionization of a hydrogen molecule by a cosmic-ray electron is associated with the deposition of 12.4 eV of heat into the gas. Thus, the heating rate per hydrogen nucleus $\Gamma_{\text{H}}/n_{\text{H}}$ is $\approx$25 eV$\times\zeta_{\text{H}}$, or about 60% of the energy loss for a single ionization of a hydrogen molecule,

$$\frac{\Gamma_{\text{H}}}{n_{\text{H}}} = 2.0 \times 10^{-26} \left(\frac{\zeta_{\text{H}}}{10^{-15} \text{ s}^{-1} \text{ H}^{-1}} \right) \text{ erg s}^{-1} \text{ H}^{-1}. \quad (4)$$

Previous estimates (Yusef-Zadeh et al. 2007b) have shown that for $n(\text{H}_2) = 5000$ cm^{-3} the equilibrium temperatures are approximately 60, 130, and 280 K for $\zeta_{\text{H}} = 10^{-15}$, 10^{-14}, and 10^{-13} s^{-1} H^{-1}, respectively (ζ_{H} is the same ζ as defined in previous section). However, what is emerging from studies of molecular clouds in the Galactic center is that the diffuse component with low density and warm gas is significant, implying that the volume filling factor of dense gas is at a 1% level (Oka et al. 2005; Dahmen et al. 1997; Sawada et al. 2001; Magnani et al. 2006). In this picture, a dense cool gas with $T < 50$ K is surrounded by a warm diffuse gas with $T > 70$ K. H$_3^+$ measurements indicate that the warm diffuse gas must have a density of $<$100 cm^{-3} (Goto et al. 2011).

To estimate the temperature of diffuse molecular gas subject to ionization by cosmic-ray electrons, we compute the cooling rate based on the calculations for $T \geqslant 100$ K by Neufeld & Kaufman (1993) and $T \leqslant 100$ K by Neufeld et al. (1995). At the densities $\sim$100 cm^{-3} of the molecular gas under consideration here, cooling is dominated by rotational transitions of CO below 100 K (e.g., Neufeld et al. 1995; Goldsmith & Langer 1978) and by rotational transitions of H$_2$ at higher temperatures (e.g., Neufeld & Kaufman 1993). The CO cooling is in the low-density, optically thin limit, with each collisional excitation radiated away by the subsequent radiative transitions down the rotational ladder back to the ground state; the cooling rate per CO molecule is therefore proportional to the H$_2$ density. Collisional de-excitation of H$_2$, on the other hand, is important even at these low densities because of the much smaller Einstein $A(s^{-1})$ coefficient values for rotational transitions. Consequently, this results in cooling by H$_2$ which is partly saturated and does not increase as strongly with density. We used spline interpolation of the CO (optically thin, low density limit) and H$_2$ rotational cooling rates tabulated by Neufeld & Kaufman (1993) and Neufeld et al. (1995) to construct the cooling function plotted in Figure 5(c). We added 0.08 dex to the CO cooling function tabulated by Neufeld & Kaufman (1993) above 100 K to eliminate a discontinuity at the 100 K boundary with the function listed by Neufeld et al. (1995).

The total cooling rate per H$_2$ molecule is plotted in Figure 5(c) for representative H$_2$ densities of 50, 100, and 200 cm^{-3}. As noted above, CO rotational cooling dominates below 100 K and scales linearly with H$_2$ density, whereas H$_2$ rotational cooling dominates above 100 K and does not scale as strongly with

increasing density. Note that the CO cooling rate is also directly proportional to the assumed CO abundance, which here is assumed to be that appropriate for gas of twice solar metallicity, i.e., $n(CO)/n(H_2) = 2.8 \times 10^{-4}$. The cooling rate can then be mapped to the cosmic-ray ionization rate that would supply heat at the same rate, and this is indicated by the right-hand axis. We see that ionization rates of 10^{-15} and 10^{-14} s^{-1} would yield gas temperatures of $\sim$100 and $\sim$200 K, respectively.

The mass of the molecular nuclear disk is estimated to be 2–6×10^7 $M_\odot$ (Oka et al. 1998; Pierce-Price et al. 2000). The diffuse molecular gas is estimated to have a density of $\sim$100 cm^{-3}, as H$_3^+$ absorption studies indicate. Assuming the gas temperature $\sim$150 K and the cosmic-ray ionization rate $\zeta \sim 5 \times 10^{-15}$ s^{-1}, Figure 5(c) gives a cooling rate 10^{-25} erg s^{-1} H$_2^{-1}$. The total energy that needs to be resupplied to keep the gas warm is estimated to be 6×10^{38} erg s^{-1}. Assuming that $\sim$10^{50} erg corresponding to 10% of the energy of a typical supernova goes into particles and the magnetic field (Duric et al. 1995), this is equivalent to one supernova per 7×10^3 years.

3.3. Ionization Fraction

One of the consequences of higher cosmic-ray ionization rate in the Galactic center environment is an increase in the ionization fraction $x_e = n_e/n_H$ in molecular clouds:

$$x_e = \frac{n_e}{n_H} \sim 10^{-7} \frac{(\zeta/10^{-17} \text{ s}^{-1})^{0.5}}{(n_H/10^4 \text{ cm}^{-3})^{0.5}}. \tag{5}$$

For typical values of $\zeta \sim 10^{-15}$ to 10^{-14} s^{-1} H^{-1}, the ratio x_e is $(1$–$3.2) \times 10^{-5}$, respectively, for a gas density of 100 cm^{-3}. Assuming an order of magnitude lower value of ζ for dense gas, the inferred value of x_e is 1–3.2×10^{-6} assuming that the gas density is 10^4 cm^{-3}. Such a high ionization fraction couples the magnetic field and the gas, and consequently slows down star formation due to an increase in the timescale for ambipolar diffusion (e.g., Yusef-Zadeh et al. 2007b). Another consequence of this interaction that can be studied in the future is the abundance of ionized molecular species such as H$_3^+$ in the Galactic center molecular clouds.

3.4. Neutral Fe I 6.4 keV Line Emission

Although the X-ray irradiation resulting from a variable fluorescent echo of the X-ray flash is considered more "favorable" to explain Fe I Kα line emission (e.g., Ponti et al. 2010), we show here that the cosmic-ray picture can also explain the 6.4 keV Kα line, especially, from molecular clouds that are considered to be interacting with nonthermal radio sources (e.g., G0.11$-$0.11). In the cosmic-ray irradiation picture, the expected low EWs of the Kα line (Yusef-Zadeh et al. 2007a) place a strong constraint on the applicability of this model for all observed clouds that show a range of low (few hundred eV) and high ($\geqslant$10^3 eV) Kα EW values. The cosmic-ray electron picture has difficulty in explaining the origin of clouds with high Kα EW values, unless Fe I abundance is increased and/or the energy index of electrons is harder in a thick target (Tatischeff et al. 2012). LECR ions interacting with molecular gas can also explain the origin of the steady Fe I 6.4 keV line emission with high EW values and no need to increase the abundance of iron (Tatischeff et al. 2012).

The remarkable distribution of diffuse fluorescent Fe I Kα line emission, as measured by *Suzaku* X-ray Observatory (Uchiyama et al. 2011), is continuous and is arising from both dense and diffuse clouds in the central molecular zone (CMZ). It is difficult to date the transient events that are responsible for production of Kα line emission from diffuse clouds. Given present observations, the cosmic-ray picture is a natural explanation. Future studies should be able to determine the relative contributions of X-ray and cosmic-ray models. Our aim here is to study the cosmic-ray electron picture which is mainly motivated by a large reservoir of cosmic-ray electrons radiating from the Galactic center at radio frequencies.

We turn to the scenario in which a high flux of relativistic particles from diffuse and localized nonthermal sources in the Galactic center inject electrons into neutral clouds. Here, we focus only on the cosmic-ray electron model which was applied to individual Galactic center clouds (Yusef-Zadeh et al. 2003, 2007a) and expand the model to the inner $2° \times 1°$ of the Galactic center. The motivations for investigating the interacting cosmic-ray picture are observationally driven since there is a large reservoir of radio emitting relativistic particles as well as a high concentration of warm molecular gas distributed in this region. Cosmic rays interact with molecular gas to produce Fe I Kα line emission, and should consequently be accompanied by an enhanced cosmic-ray ionization rate and elevated molecular gas temperature.

3.4.1. The Low-energy Cosmic-ray Model

The role of LECR electrons in producing X-rays has been discussed in the context of impulsive solar flares (Zarro et al. 1992) and the background X-ray emission from the Galaxy (Valinia et al. 2000). An LECR electron model was subsequently applied to the 6.4 keV X-ray emission from the Galactic center molecular cloud G0.11–0.11 (Yusef-Zadeh et al. 2002). The emission was explained in terms of the impact of LECR electrons with neutral gas associated with the G0.11−0.11 molecular cloud.

To investigate the applicability of the cosmic-ray interaction, we made a systematic study of molecular clouds showing fluorescent 6.4 keV line emission (Yusef-Zadeh et al. 2007a). We present below a strong spatial correlation between nonthermal radio sources and molecular clouds. We account for the distribution of Fe I Kα line emission arising from relativistic particles diffusing from both nonthermal filaments and compact nonthermal sources and impacting on neutral gas, producing both nonthermal X-ray bremsstrahlung and 6.4 keV line emission. The energy density of LECRs was estimated to be in the range 20 to $\sim$10^3 eV cm^{-3} for all Galactic center clouds (Yusef-Zadeh et al. 2007a).

The production rate of Fe I Kα photons depends on the electron spectral index and iron abundance. For a given particle spectral index p, the efficiency of Kα production q increases with column density, eventually flattening when the column is sufficient to stop the bulk of the injected electrons within the cloud. Figure 6(a) shows the dependence of Fe Kα production per erg of electron energy injected into a cloud with column density N_H for different values of the electron energy spectral index p. The curves indicate that hard particle spectra ($p = 1$–1.5) show high efficiency of producing Kα line emission corresponding to high column densities, whereas the soft particle spectra ($p = 2.5$–3) show high efficiency at low column densities. Steeper spectra have particle energies increasingly concentrated toward low energies and so the flattening of the Kα production rate occurs at successively lower column densities. However, for the range of column densities between 10^{23} and 7×10^{24}, electrons with the power-law energy index $p = 2$ are most efficient in producing Kα line emission. This spectrum has equal energy
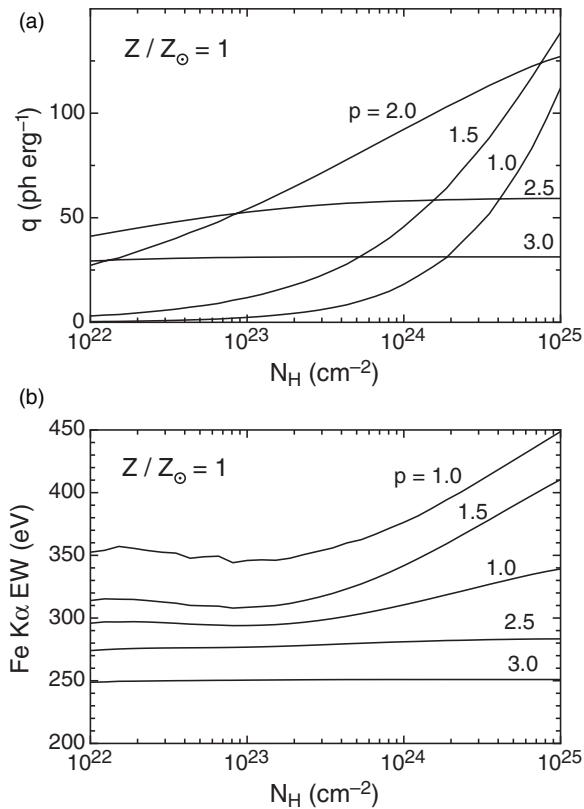
Figure 6. (a) Fe Kα production per erg of electron energy injected into a cloud of given column density N_H and a solar iron abundance (Fe/H = 2.8×10^{-5}). The curves are labeled by the power-law index p of the electron energy spectrum ($\propto E^{-p}$), which is assumed to run from 10 keV to 1 GeV. (b) Similar to (a) except that the EW of Fe Kα is shown as a function of column density for different values of the energy spectral index.

per decade between 10 keV and 1 GeV, or energy density is the same in each frequency decade. We conclude that typically $q \sim 50 \, z/z_\odot$ photons erg^{-1}, where z is the metallicity and $z_\odot$ is the solar metallicity, for typical spectral indices and cloud column densities, increasing to $\sim 100 \, z/z_\odot$ for hard electron spectra and high column densities, as observed in the Galactic center.

In order to determine the EW of Kα line emission, the bremsstrahlung emission at 6.4 keV was also estimated, as plotted in Figure 6(b). For $z = z_\odot$, the EW varies between 250 and 450 eV for particle spectral index p varying between 3 and 1. There is a dependence of EW on column density in excess of 10^{24} cm^{-2}, where we note an increase in EW for hard particle spectra. A similar study also concluded that the EW of Fe I Kα line emission at 6.4 keV produced by electrons having a hard spectrum $p = 1.5$ ranges between 450 and 500 eV for high column density of 10^{25}–10^{24} cm^{-2}, respectively (see Figure 4 of Tatischeff et al. 2012). These parameters apply to Galactic center clouds since the spectrum of electrons at low energies is hard and the column density of neutral gas is generally high in this region.

We apply the LECR model to the inner $2° \times 0°.85$ by estimating the Kα line and bremsstrahlung emission from the interaction of the extrapolated low-energy tail of the nonthermal electrons responsible for synchrotron radio emission. We assume that the nonthermal radio emission is produced by a power-law spectrum $n(E) \propto E^{-p}$ of electron energies between 10 keV and 1 GeV, and that the depth of the emitting region is of the order of its diameter 288 pc and calculate the energy density of cosmic-

ray electrons assuming that they are in equipartition with the magnetic field.

First, we note that the interaction of these electrons simultaneously heats and ionizes the cloud, as well as giving rise to fluorescent emission in the Kα line due to the ejection of inner K-shell electrons from Fe I. Noting that each ionization is associated with deposition of energy $W \approx 40.1$ eV in the cloud and that q Kα photons are produced for each erg deposited, the Kα photon production rate per hydrogen nucleus is $qW\zeta$ photons s^{-1} H^{-1} where W is expressed in erg. The intensity of Kα photons received from a hydrogen column N_H subject to a cosmic-ray-electron-induced ionization rate per hydrogen nucleus ζ is then

$$I_{K\alpha} = \frac{qW\zeta \, N_H}{4\pi} \approx 8.7 \times 10^{-8} \left(\frac{\zeta}{10^{-14} \, \text{s}^{-1}} \right)$$
$$\times \left(\frac{N_H}{10^{23} \, \text{cm}^{-2}} \right) \text{photons s}^{-1} \, \text{cm}^{-2} \, \text{arcmin}^{-2} , \quad (6)$$

where we have assumed $q = 200$ photons erg^{-1}, corresponding to a metallicity twice solar. The unabsorbed Fe I Kα photon flux determined by *Suzaku* observations is about 3.8×10^{-7} photons s^{-1} cm^{-2} arcmin^{-2} (Uchiyama et al. 2011). Typical Galactic center clouds such as Sgr C have column densities in the range 3–8×10^{23} cm^{-2} (e.g., Yusef-Zadeh et al. 2007a). Adopting a typical value $N_H = 4 \times 10^{23}$ cm^{-2}, we infer that the required ionization rate $\zeta \sim 10^{-14}$ s^{-1} H^{-1}.

This cosmic-ray ionization rate can be compared with the minimum value of the product of the cosmic-ray ionization rate and the path length L in diffuse molecular gas determined by H$_3^+$ absorption measurements over eight sight lines toward the Galactic center (see Table 4 of Goto et al. 2008). The average minimum value of ζL is $\sim 1.2 \times 10^5$ cm s^{-1} H^{-1}. Multiplying ζL by the density of neutral gas $n(\text{H}_2) \sim 100$ cm^{-3} inferred from the H$_3^+$ measurements and comparing this to ζN_H, we estimate that the diffuse molecular gas component responsible for the H$_3^+$ absorption contributes about 10% of the Fe I Kα line emission at 6.4 keV. The remaining 90% of the 6.4 keV emission can be explained by the interaction of electrons with $\sim 10^3$ cm^{-3} molecular gas. Thus, the cosmic-ray ionized rates inferred from H$_3^+$ and Fe I Kα line emission probe diffuse and dense phases of the molecular ISM, respectively. This is consistent with ammonia measurements that also infer a two-phase structure to the molecular gas based on a bimodal temperature distribution within Galactic center molecular clouds (Hüttemeister et al. 1993).

The contribution of protons has been ignored here, but can also be significant (see Tatischeff et al. 2012). In a thick target, the efficiency of producing the 6.4 keV line emission is similar for both protons and electrons with energies ~ 20–200 MeV and ~ 10–100 keV, respectively. For proton-to-electron ratios of 40, the production of the 6.4 keV line emission could be as important as electrons as long as the spectrum of the particles is hard (see Figures 6 and 13 of Tatischeff et al. 2012).

Another important issue is the energetics required by this picture. The total energy of cosmic-ray electrons contained within a volume of $2° \times 2° \times 0°.85$ is 2.7×10^{50} erg, assuming that the observed radio flux comes from an oblate spheroid with the emission having a volume filling factor of 0.1 and that the electrons are in equipartition with a 20 μG field. The Kα flux emitted over the inner $2° \times 1°$ is estimated to be 2.7×10^{-3} photons cm^{-2} s^{-1} (Uchiyama et al. 2011), corresponding to a 6.4 keV luminosity $\sim 2 \times 10^{35}$ erg s^{-1}. Given that the

efficiency for producing the Fe I Kα line by cosmic-ray electron impacts is $\sim 2 \times 10^{-6}$ (Tatischeff et al. 2012), the total kinetic power lost by the LECR electron population is $\sim 10^{41}$ erg s^{-1}. This implies that the electrons depositing their energies onto molecular clouds from the inner $2° \times 1°$ must be resupplied on a 100 year timescale. A longer timescale can be achieved if the electrons that lose their energies are resupplied by the leakage of cosmic rays. In this picture, a higher fraction of the electrons will interact with molecular gas and the electrons need to be resupplied on a longer timescale of $\sim 10^3$ years. The timescale estimate could be a lower limit as the average Kα line at 6.4 keV surface brightness could be lower than that estimated here due to contamination by unresolved point sources. In addition, transient X-ray sources such as Sgr A* could have contributed in producing a fraction of the Fe I Kα line emission.

3.4.2. The Correlation of Fe I Kα Line and Radio Continuum Emission

The production of Fe I Kα line emission in the LECR scenario implies a correlation between the distribution of nonthermal radio continuum and Fe I Kα line emission. Combining Equations (3) and (6) yields

$$I_{K\alpha} \approx \frac{2.7 \times 10^{-7}}{p-1} \frac{I_\nu}{\text{Jy arcmin}^{-2}} \left(\frac{\nu}{\text{GHz}}\right)^\alpha \left(\frac{B}{100\,\mu\text{G}}\right)^{-(1+\alpha)}$$
$$\times \left(\frac{N_\text{H}}{10^{23}\,\text{cm}^{-2}}\right)\left(\frac{L}{30\,\text{pc}}\right)^{-1} \text{photons s}^{-1}\,\text{cm}^{-2}\,\text{arcmin}^{-2},$$

(7)

where we have again adopted $q = 200$ photons erg^{-1} for the efficiency of Kα production.

To test this correlation, we used the intensity of Kα line emission listed in Table 2 of Uchiyama et al. (2011) and compared with radio emission at 325 MHz based on combined GBT and Very Large Array (VLA) data. We convolved the 325 GHz map by a $6' \times 6'$ Gaussian before it was compared with *Suzaku* data. Figures 7(a)–(i) show nine crosscut plots of X-ray and radio data made in the direction parallel (Figure 7(a)) and perpendicular (Figures 7(b)–(i)) to the Galactic plane. Given that there is contamination by thermal radio continuum sources at 325 MHz, these plots suggest that the flux of nonthermal continuum emission does indeed track the 6.4 keV line flux, as predicted by Equation (7). For a typical flux of 50 Jy at 325 MHz and $p = 1.4$, the predicted Kα line intensity is $\sim 2 \times 10^{-7}$ photons s^{-1} cm^{-2} arcmin^{-2} which is similar to what has been observed in most plots shown in Figure 7. The radio flux in Figure 7(a) shows the highest value of ~ 250 Jy but Kα intensity is similar to the values shown in a typical slice. The peak radio flux mainly arises from the strong radio emission associated with Sgr A East where Kα line intensity is weak. The well-known Sgr A East supernova remnant is known to be interacting with the 50 km s^{-1} molecular cloud. The clouds that show a lack of 6.4 keV emission in the context of the cosmic-ray irradiation picture have either a low column density for production of X-ray photons or a high extinction inside a dense cloud that substantially reduces the flux of Kα emission. The 50 km s^{-1} molecular is one example in which the column density is sufficiently large for extinction to reduce the emission. Column densities ranging between ~ 5–10×10^{23} cm^{-2} reduce the X-ray flux at 6.4 keV by a factor of 2–5 and 5.6–31 for one and two times solar metallicity, respectively (Morrison & McCammon 1983). The assumption that all of synchrotron

emitting particles interact with molecular gas can also contribute to explaining this discrepancy. If only a fraction of the electrons interact with molecular gas, the radio flux in Equation (6) will be smaller, and thus the flux of the Kα line will be reduced. Lastly, the timescale for the variability of 6.4 keV line emission is relatively short in the case where electrons propagate through a dense molecular cloud. Thus, the discrepancy can be explained by a combination of effects that can potentially suppress the 6.4 keV line emission from dense clouds with high column densities. However, if the metallicity is twice solar in the 50 km s^{-1} cloud, the extinction could be the dominant effect in suppressing the 6.4 keV emission.

3.4.3. EW Distribution of Fe I Kα Line Emission

One of the key parameters that can distinguish LECR and X-ray irradiation scenarios of Fe I Kα line production is the strength of the EW of Fe I Kα line. The large EW $\sim 10^3$ eV is more consistent with the X-ray irradiation picture of producing Fe I Kα emission (Sunyaev & Churazov 1998), whereas the low EW of about few hundred is more consistent with that of the cosmic-ray irradiation picture. Given that both emission mechanisms depend on the abundance of Fe I, the predicted EWs should be higher in the Galactic center due to an increase in the metallicity gradient toward the Galactic center (Giveon et al. 2002; Rudolph et al. 2006). Recently, spectral analysis of emission lines from several neutral atoms based on *Suzaku* observations showed the EW of Kα line emission at 6.4 keV to be ~ 1.1 keV (Nobukawa et al. 2010). Figure 8(a) shows a grayscale distribution of the 6.4 Kα line emission based on *Chandra* observations with a resolution of $2''$. Figure 8(b) shows contours of the EW superimposed on a 20 cm continuum image of the Galactic center. A range of EWs are noted between ~ 100 and $\sim 2 \times 10^3$ eV associated with Galactic center molecular clouds. These images show a number of compact sources with high value of EWs (e.g., Sgr B2, the Arches cluster) as well as large diffuse structures associated with extended molecular clouds. The low EW distribution of the Fe I Kα line emission suggests that diffuse envelopes are consistent with typical EW values expected in the context of bombardment of cosmic-ray and X-ray photon irradiation. Recent work shows that LECR electrons can produce a significant Fe I Kα line emission from diffuse molecular clouds with $N_\text{H} < 10^{22}$ cm^{-2}, especially in clouds with strong particle diffusion (see Figure 4(b) of Tatischeff et al. 2012). An observation of a 6.4 keV line emission from a cloud with $N_\text{H} \sim 10^{21}$ cm^{-2} is potentially a promising signature of LECR electrons, as the efficiency of production of this line by hard X-ray irradiation of the cloud is low (Yaqoob et al. 2010). For higher values of the EW, the Fe abundance in the gas phase or in dust has to increase in order to be consistent with the LECR electron model.

3.4.4. Comparison of EW: Chandra versus Suzaku

We also measured the EW distribution using *Suzaku* with its moderate resolution from the same region shown in Figure 8. *Suzaku* data are sensitive to diffuse 6.4 keV line emission whereas *Chandra* data are clearly able to identify compact features in the EW distribution. The contribution of point sources have been removed in the *Chandra* image before the EW map is constructed. To compare these two different measurements, we show several crosscuts parallel to the Galactic ridge at constant latitudes. Figure 9 shows plots of these crosscuts in blue and red corresponding to *Suzaku* and *Chandra* measurements. We also averaged the EW over longitude intervals
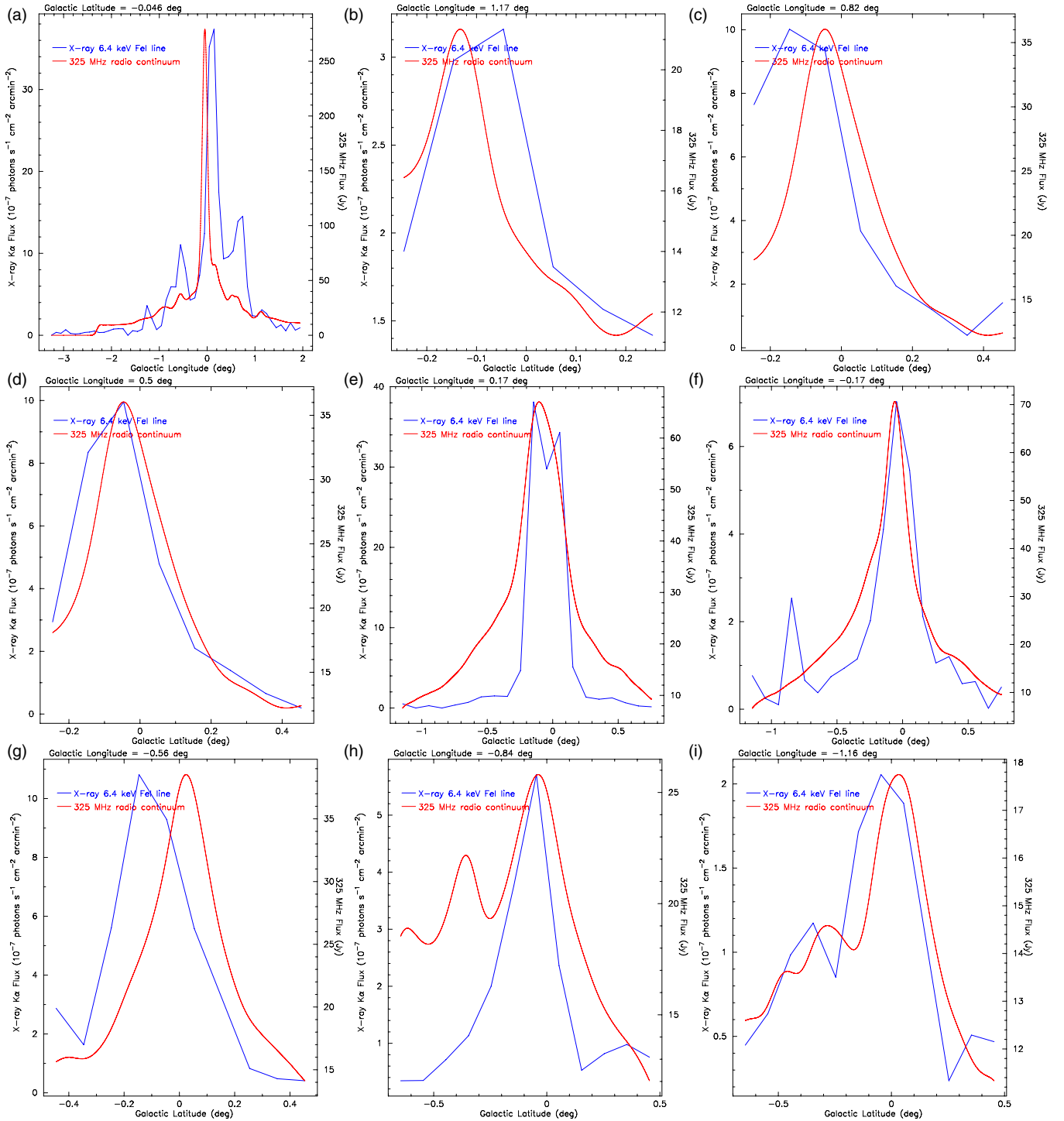
Figure 7. (a–i) Cross cuts made on the distribution of Kα line (blue) and 325 MHz (red) with different position angles. The 325 MHz data are based on GBT and VLA observations that have been combined before the map was convolved with a 6′ Gaussian in order to match the distribution of X-ray flux measured with *Suzaku*. There is one cross cut at constant latitude $b = -0°.046$ shown in (a) whereas eight other cross cuts are shown in (b–i) corresponding to constant longitudes.
(A color version of this figure is available in the online journal.)

of 3′ and made a one-dimensional distribution of EW based on *Suzaku* and *Chandra*. Both *Chandra* and *Suzaku* data indicate that the EW values vary substantially in the Galactic center from a few hundred eV to close to 1–2 keV. The EW profiles were binned by averaging over 4′ and the variation from the mean for both *Chandra* and *Suzaku* data are consistent with each other. However, there is an offset EW ~ 100–150 eV in the mean value the EW that is present especially at higher galactic latitudes.

Chandra data are averaging over low-intensity pixels that have no available data in *Suzaku* measurements. This is because the spatial coverage of *Suzaku* observation measurements was not uniform. Additional cause of this discrepancy could be due to the uncertainty of properly subtracting the hot background continuum emission (Koyama et al. 2009) in the construction of the 6.4 keV EW map based on *Chandra* observations, as described in Section 2.5.1. In a recent study of the Galactic center, the
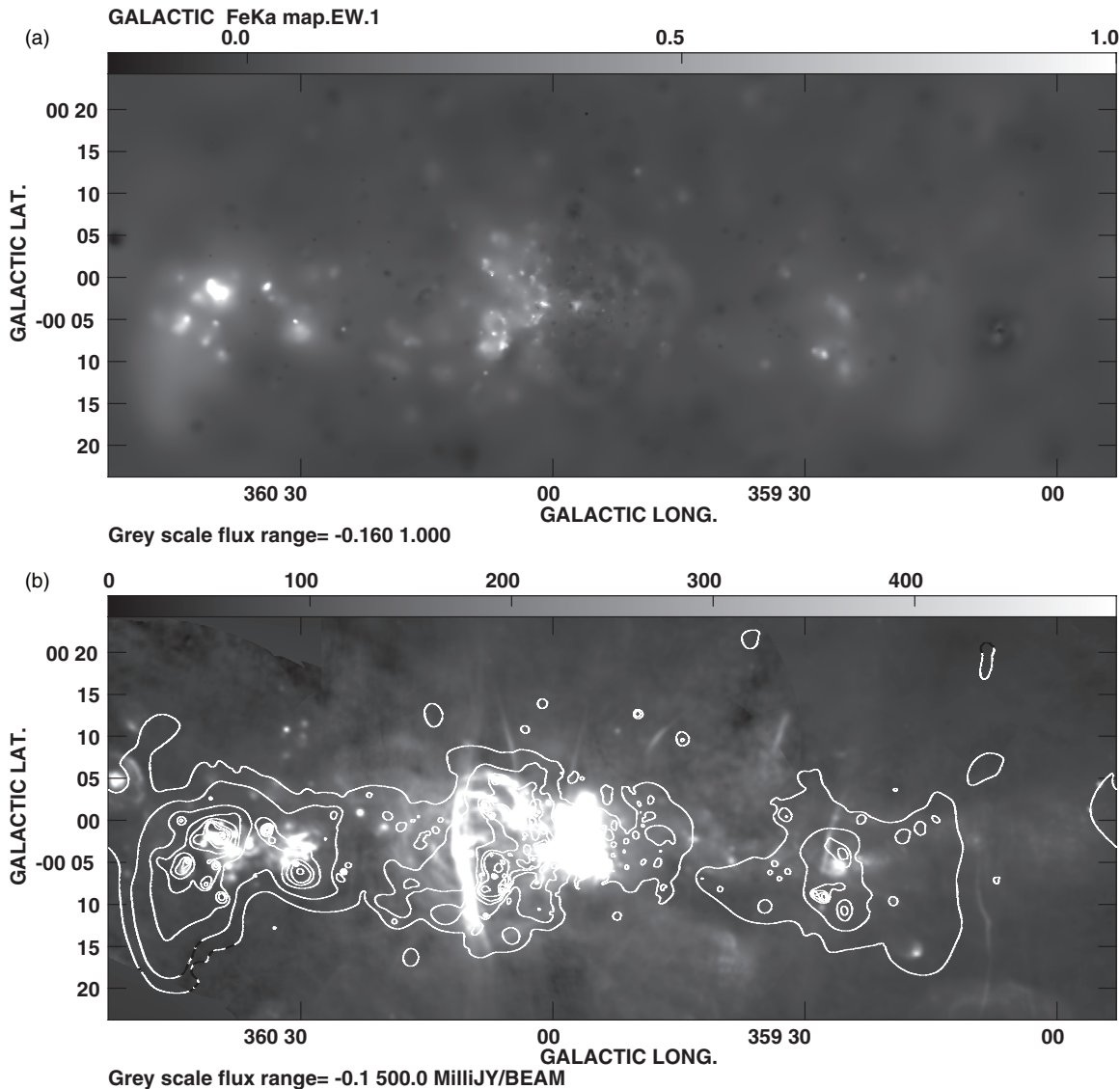
Figure 8. (a) An adaptively smoothed gray-scale image of the EW of Fe I Kα line emission from the inner $-0°.8 < l < 0°.7$. The range is between 50 and $2 × 10^3$ eV. (b) Contours of the EW of Fe I Kα line emission with values set at $100×$ (0.5, 1, 2, 3, 4, 6, 8, 10, 14, 18, and 20) eVs are superimposed on a gray-scale continuum image at 1.4 GHz with a resolution of 30″.

anti-correlation between the EW values of the 6.7 and 6.4 keV line emission based on *Suzaku* measurements suggests that the EW value of 6.4 keV line emission, when averaged over the region $-2° < l < 1°$, is about 700 eV which is more consistent with *Suzaku* measurements shown in Figure 9 (Uchiyama et al. 2011). These measurements suggest that the low value of the EWs can be explained in the context of the cosmic-ray model or a mixture of cosmic-ray and X-ray echo models. As pointed out earlier, our radio continuum observations of the inner $2° ×$ $1°$ suggest that the energy spectrum of cosmic-ray electrons is ~ 1.5 and that the column density is $\geqslant 10^{23}$ cm^{-2}. Under these conditions, the typical EW is predicted to be about 450 eV for solar abundance of Fe I Kα line emission. In this case, the spectrum of injected particles diffusing into a cloud with a higher metallicity can account for high and low values of the EW.

3.4.5. Radio Arc and G0.11−0.11 (or G0.13−0.13)

One of the most interesting Galactic center molecular clouds showing strong 6.4 keV emission is G0.11−0.11 which is positioned at the edge of the nonthermal filaments of the Arc.

Thus, it is an important cloud as it can be used to test the cosmic-ray irradiation picture. Figure 10(a) shows contours of the EW (eV) based on *Chandra* observations and are superimposed on a gray-scale continuum image at 20 cm. This figure illustrates the long nonthermal radio filaments that run perpendicular to the Galactic plane. Figure 10(b) shows the same region of the sky as that of Figure 10(a) except that contours of the Kα line emission are superimposed on a gray-scale Kα line image. The morphology of the eastern edge of the G0.11−0.1 molecular cloud led Tsuboi et al. (1997) to argue that radio filaments and G0.11−0.11 are dynamically interacting with each other. The EW ranges between ~ 110 and ~ 1100 eV peaking on diffuse and compact sources within the G0.11−0.11 cloud. The low value of the EW of Kα line emission is consistent with the interaction picture. The high value of the EW of Fe I 6.4 keV line toward G0.11−0.11 requires us to have a high abundance of iron. It is interesting that spectroscopic studies of gas toward the radio Arc bubble immediately adjacent the G0.11−0.011 cloud shows a 6.5-fold increase in the abundance of iron in the gas phase compared to the surrounding ISM (Simpson et al.
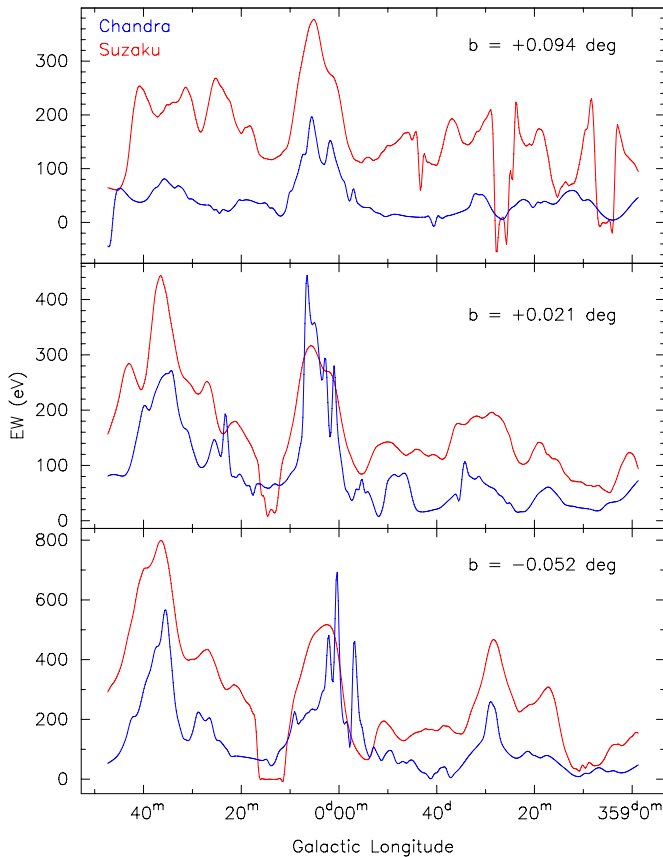
Figure 9. Plots of cross cuts of EW as a function of Galactic longitudes at three different latitudes, in blue and red corresponding to *Chandra* and *Suzaku* measurements. Each slice is an average of all the data in 4′ of galactic latitude and a range of galactic longitude divided in 19 steps between $l = 53'$ and $l = -53'$. A part of the *Suzaku* data is missing because regions of bright point sources, 2E 1743.1−2842, 2E 1742.9−2929, and 2E 1740.7−2943, are masked. (A color version of this figure is available in the online journal.)

2007). Using the observed value of the EW toward G0.11−0.11 (Nobukawa et al. 2010), we find that the Fe abundance has to be ⩾2.2 in the context of the LECR picture.

Another isolated cloud at the edge of the nonthermal filaments in Figures 10(a) and (b) shows a cloud with a low value of Kα line emission. This cloud G0.16−0.22 coincides with recent *Suzaku* observations which first reported the discovery of Kα line emission (Fukuoka et al. 2009), lying at the southern end of the nonthermal filaments. The low value of the EW led them to suggest that cosmic-ray irradiation by electrons is responsible for 6.4 keV emission. Our *Chandra* measurements are consistent with the low value of EW, which peaks at ∼130 eV.

Another interesting 6.4 keV cloud revealed in Figure 10 is the presence of Kα line emission peaking at the location where the longest nonthermal radio filament (Figure 10(a)) crosses the well-known Sickle H II region G0.18−0.04 (Yusef-Zadeh & Morris 1987) at $l = 10.6$, $b = -3'$. This peak has EW ∼ 200 eV and lies at the interface of nonthermal filaments and the 40 km s^{-1} molecular cloud which is associated with the Sickle. The kinematics of ionized gas exactly at the interface between nonthermal filaments and the Sickle at G0.18−0.04 shows a forbidden velocity of −30 km s^{-1} (Yusef-Zadeh et al. 1997). This anomalous motion of ionized gas in the Sickle can be interpreted in the context of the interaction of the magnetized filaments and the 40 km s^{-1} cloud. A more detailed account of

this result which is consistent with the cosmic-ray interaction picture will be given elsewhere.

3.4.6. Time Variability of Fe I Kα Line Emission

One of the key issues related to the cosmic-ray interaction picture in the Galactic center is the observed time variability of Fe I Kα emission from several clouds (Inui et al. 2009; Terrier et al. 2010; Ponti et al. 2010). Although the echo X-ray picture can explain the variable emission well, it turns out that the cosmic-ray electrons' picture can also explain this remarkable property of Galactic center molecular clouds. In the cosmic-ray picture, the flux of electrons diffuses from their acceleration site to the cloud edge, and then freely streams into the cloud because ion–neutral damping suppresses the magnetic fluctuations responsible for the diffusion. As the electrons penetrate molecular clouds, the timescale for energy loss of electrons at low energies is quite rapid. Consequently, the energy spectrum of particles become harder.

As a demonstration of this idea, Figure 11(a) shows spectra of LECR electrons propagating in a medium of density $n_H = 10^4$ cm^{-3}, over a time interval that is very short compared to the lifetime against energy losses. The energy spectrum of electrons is assumed to have a power-law energy spectral index $p = 2.4$ above a minimum energy $E_{min} = 100$ keV and $E_{max} = 1$ GeV. The electrons of energies less than E_{min} are expected not to escape their acceleration region and do not penetrate into molecular clouds. The normalized electron injection spectrum corresponds to the total electron energy content of 10^{48} erg. Since the electrons losses are proportional to the density, if we choose a number density $n_H = 100$ cm^{-3}, then the energy loss timescale increases by a factor of 100. The energy loss timescale also depends on the energy spectrum of electrons. For a harder spectrum of electrons $p = 1$, the energy loss timescale does not vary as fast as shown in Figure 11(a). So for $n_H = 100$ cm^{-3}, the typical timescale of evolution is 100 years, and any significant variation in the 6.4 keV line emission on shorter timescales would rule this model out.

Figure 11(b) shows nonthermal X-ray spectra produced by LECR electrons with the assumption that the metallicity of the ambient medium is twice solar. We have accounted for photoelectric absorption along the line of sight with a hydrogen column density $N_H = 6 \times 10^{22}$ cm^{-2}. We have ignored the Fe I Kα line emission generated by the impact of secondary electrons. These electrons can account for no more than 20% of X-ray emission. The observed variability measurements toward dense clouds, such as G0.11−0.11 and Sgr B2, are consistent with the prediction of flux variability of the 6.4 keV line, as presented in Figure 11(b).

Lastly, Figure 11(c) shows the time evolution of the EW of the neutral Fe Kα line and the luminosity in this line. To illustrate how the time evolution of X-ray luminosity varies, the injected spectrum of electrons are varied between $p = 1.5$ and 2.4 as well as different minimum energies 10 and 100 keV. In the bottom panel of Figure 11(c), we note a constant luminosity of ∼10^{42} photons s^{-1} corresponding to ∼3×10^{-4} photons cm^{-2} s^{-1} at 8 kpc followed by a decrease in time as ∼$t^{-1.2}$. The top panel shows that the EW of the 6.4 keV line stays almost constant at 0.8 keV. These figures show clearly that the interaction of LECR particles with ambient gas can produce a fast variability of the Fe I Kα line emission at 6.4 keV. There are numerous nonthermal radio filaments distributed in the Galactic center region, some of which will be interacting with molecular gas in this region. At the site of the interaction,
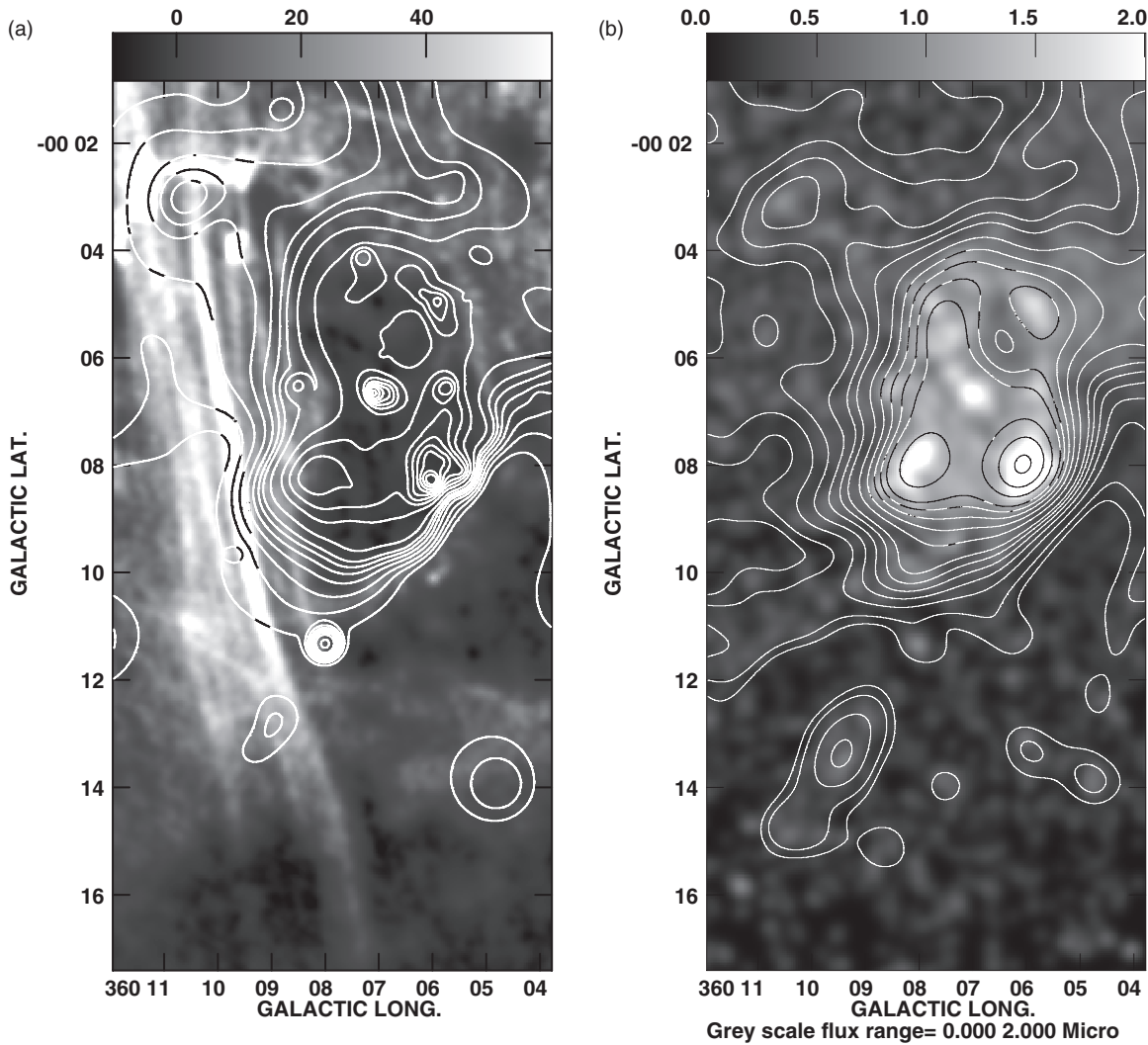
Figure 10. (a) Contours of EW based on *Chandra* observations with levels set at 110, 130, 150, 175, 200, 225, 250, 300, 400, 500, 600, 700, 800, 900, 1000, 1100 eV are superimposed on a gray-scale continuum image at 1.415 GHz based on VLA observations. (b) Contours and gray scale distributions of Kα line emission are shown for comparison with (a).

the nonthermal electrons are impulsively injected into the cloud as they follow the distorted magnetic field lines. In this picture, the injected particles lose their energies on a timescale that is similar to the observed decay timescale of Kα line emission. The particles diffusing into the cloud are not resupplied. Another consequence of the cosmic-ray interaction picture is that the value of ζL measured from H_3^+ absorption study should be time variable. This is because LECR electrons are responsible for production of this important ionized molecule.

Another possibility that could account for the variability of Kα line emission is to accelerate electrons to TeV energies at the interface of the interaction. *Chandra* observations detected a filamentary X-ray structure (G0.13−0.11) sandwiched between nonthermal radio filaments of the Arc and the 6.4 keV line emission from the extended molecular cloud G0.11−0.11 molecular gas (Yusef-Zadeh et al. 2002). This filament has a photon index $\Gamma = 1.4$–1.5 (Wang et al. 2002a; Johnson et al. 2009). The nature of this filament, which has neither 6.4 keV line nor radio continuum counterparts, suggests that the nonthermal X-ray emission is consistent with a synchrotron emission from electrons with TeV energies. The variability of the emission due to short synchrotron lifetimes place strong constraints on the energy and the

magnetic field of the particles at the interaction site. For example, for $E = 4$ TeV, $B = 1$ mG, $t_{synch} \sim 2$ years at 1 keV energies. The variable X-ray emission at the site of the interaction could in principle produce the variable X-ray fluorescent line emission detected from G0.11−0.11. This should be observed in future X-ray observations.

4. DIFFUSE GeV AND TeV γ-RAY EMISSION

In previous sections, we have argued that the interaction of cosmic-ray electrons with the gas in the Galactic center can explain the measured high values of cosmic-ray ionization and heating rates. We also explained that the interacting low-energy tail of cosmic-ray particles contributes nonthermal bremsstrahlung continuum emission as well as the Fe I Kα line at 6.4 keV. We now examine whether nonthermal bremsstrahlung from a population of synchrotron emitting electrons in the Galactic center can explain the GeV and TeV γ-ray emission from the Galactic center.

Recent observations with the H.E.S.S. have discovered large-scale diffuse TeV emission from the inner 200 pc of the Galaxy (Aharonian et al. 2006). The morphology of diffuse emission
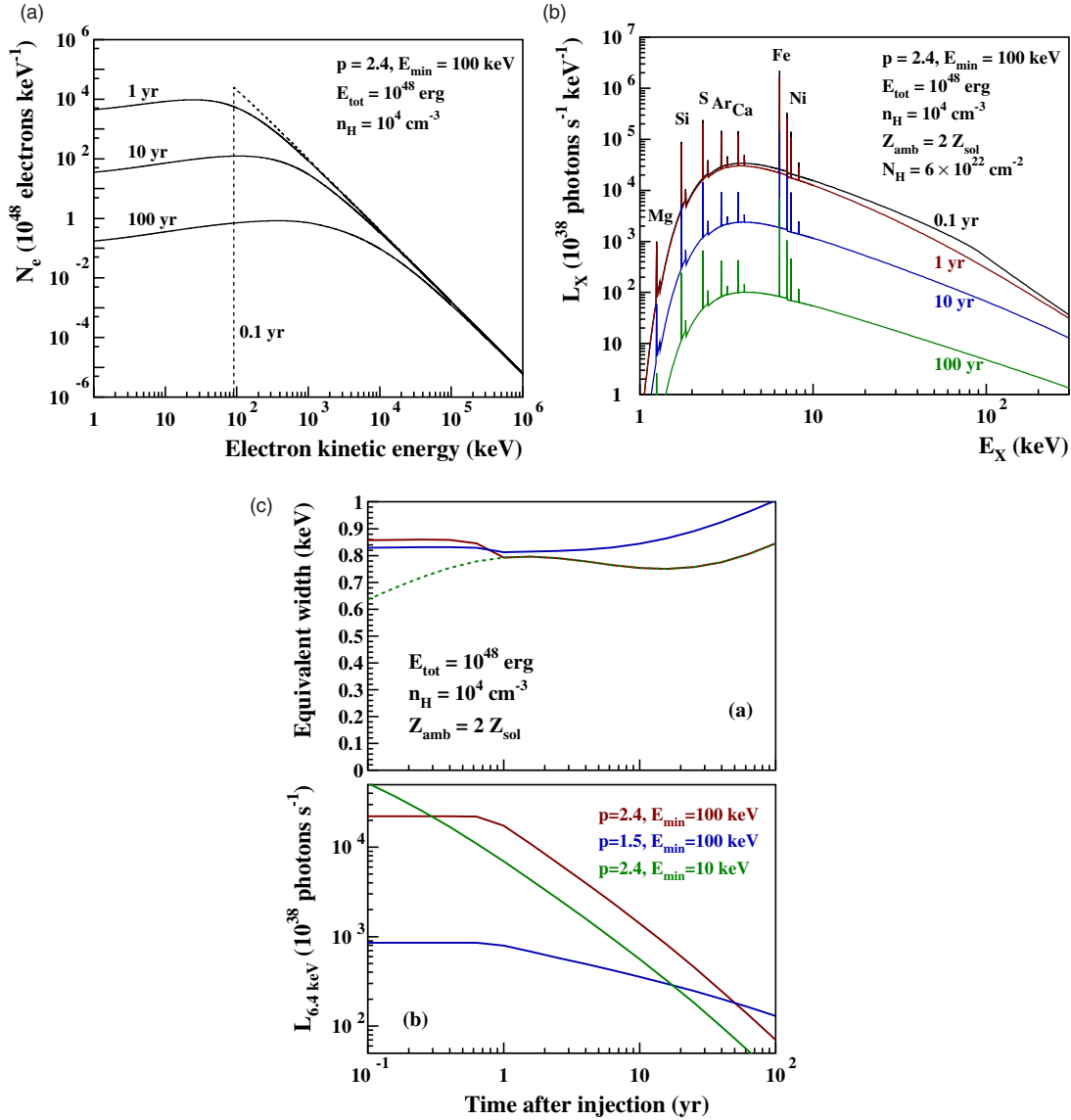
Figure 11. (a) The energy loss of electrons in a medium with ambient density of 10^4 cm^{-3} are shown after 1, 10, and 100 years. The initial spectrum with a power-law distribution is shown as a dotted line between low- and high-energy cutoffs of 100 keV and 1 GeV, respectively. (b) Nonthermal X-ray spectra produced by LECR electrons with the assumption that the metallicity of the ambient medium is twice solar. Photoelectric absorption along the line of sight with a column density $N_H = 6 \times 10^{22}$ cm^{-2} has been assumed. (c) The top panel shows the time evolution of the EW of the neutral Fe I Kα line whereas the bottom panel shows the luminosity in the 6.4 keV line.

(A color version of this figure is available in the online journal.)

correlates well with the distribution of CS molecular clouds, thus suggesting that the γ-ray emission is a product of the interaction of cosmic rays with interstellar gas near the Galactic center. These authors show that the spectrum of TeV emission from resolved clouds toward the Galactic center has a photon index $\Gamma \sim 2.3$ which is harder than that in the Galactic disk. They note that the γ-ray flux above 1 TeV is a factor of 3–9 times higher than in the Galactic disk and argue for an additional population of cosmic rays in this unique region. They propose that the TeV emission is due to hadronic interaction of cosmic rays with the target material. Given that the target material is the same, we recently argued (Yusef-Zadeh et al. 2007a) a spatial correlation between the distribution of TeV emission with those of the 6.4 keV emission and submillimeter emission tracing molecular gas toward the Galactic center. An argument against the importance of TeV electrons in Sgr B2 is the short lifetime of few decades for their energies

with a magnetic field of an order of 0.5 mG (Crocker et al. 2010).

Morphological distribution of diffuse γ-ray emission detected by *Fermi* is remarkably similar to that of radio continuum emission at 1.45 GHz, as shown in Figures 4(a) and (b). It is also known that the distribution of TeV emission traces Galactic center molecular clouds. These correlations suggest that the γ-ray emission is a product of the interaction of cosmic rays with interstellar gas near the Galactic center. Adopting a power-law electron energy spectrum E^{-p} (Schlickeiser 2003), the bremsstrahlung photon flux is

$$F_\gamma \approx \frac{3.3 \times 10^{-13}}{p - 1} \left(\frac{S_\nu}{\text{Jy}}\right) \left(\frac{\nu}{\text{GHz}}\right)^\alpha \left(\frac{B}{100\,\mu\text{G}}\right)^{-(1+\alpha)} \left(\frac{n_H}{\text{cm}^{-3}}\right)$$
$$\times \left(\frac{E_\gamma}{1\,\text{GeV}}\right)^{-p} \text{photons cm}^{-2}\,\text{s}^{-1}\,\text{GeV}^{-1}, \quad (8)$$
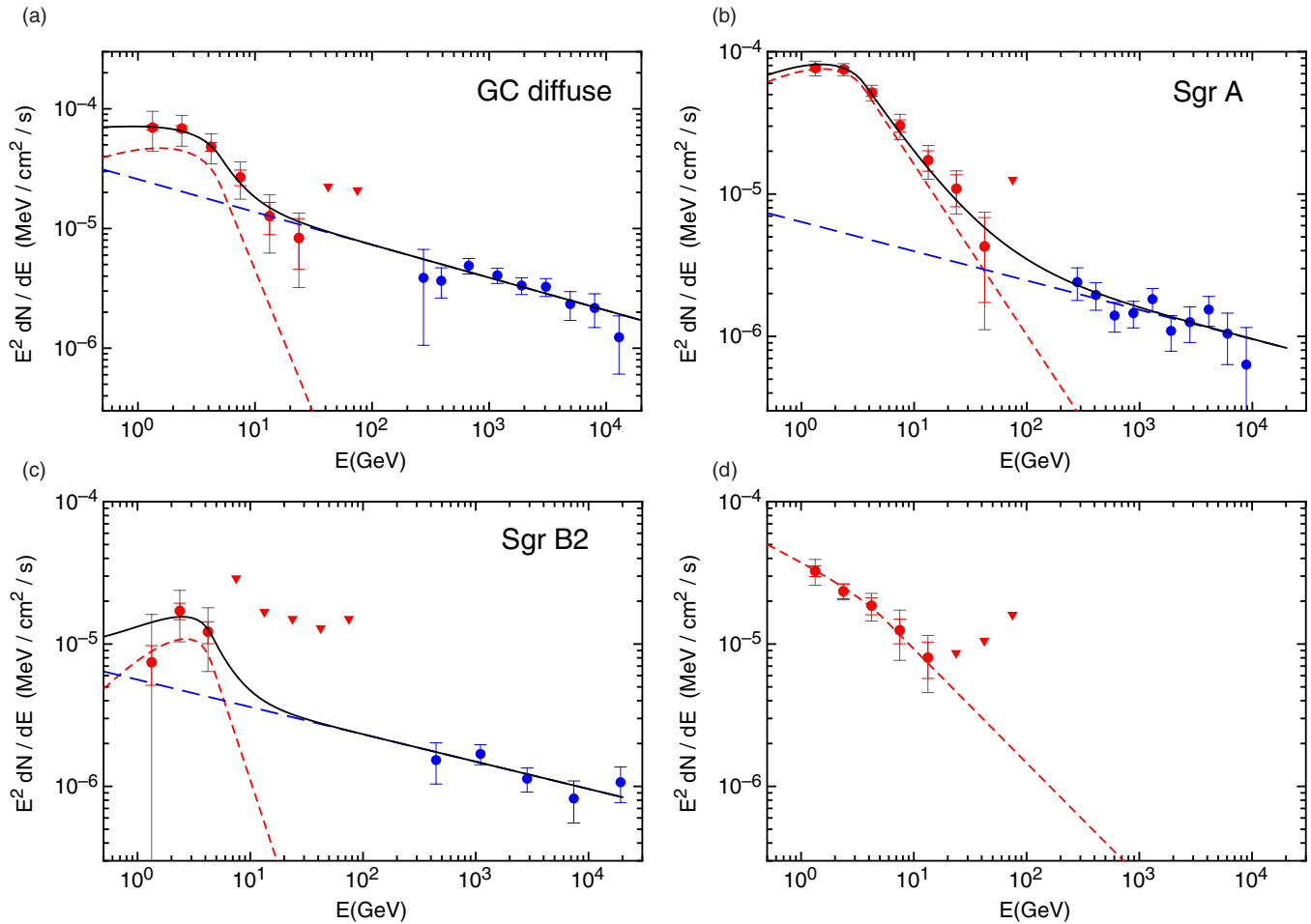
Figure 12. (a) The plot for Galactic center diffuse emission shows *Fermi* and H.E.S.S. data points in red and blue, respectively. Red triangles show 3σ upper limits of *Fermi* data points. The red dashed curve is the γ-ray bremsstrahlung predicted from nonthermal radio spectrum using two different spectral index values. The blue dashed line shows power-law fit to the H.E.S.S. data. The black solid curve is the sum of the two bremsstrahlung contributions. (b) Similar to (a) except that the plot shows the spectrum of γ-ray emission from Sgr A. (c) Similar to (a) except that the plot shows the spectrum of γ-ray emission from Sgr B2. (d) Similar to (a) except that the plot shows the spectrum of γ-ray emission from the radio Arc. There is no H.E.S.S. data for this source. The parameters of the fit to all the plots are given in Table 4.

(A color version of this figure is available in the online journal.)

where E_γ is the photon energy in GeV, ν is the synchrotron observing frequency in GHz, s_ν is synchrotron flux, and $n_H = n(H\,I) + 2n(H_2)$ is the number density of hydrogen nuclei in atomic or molecular form, in cm^{-3}. We assume here that all of the synchrotron-emitting electrons are interacting with the gas.

We interpret the *Fermi* and H.E.S.S. data in the context of nonthermal bremsstrahlung radiation mechanism. We present the spectra from several sources from the inner $2° \times 1°$ of the Galactic center. Figure 12(a) shows the spectrum of the diffuse emission from the inner $2° \times 1°$ by excluding the source that lies very near Sgr A*. This spectrum includes both *Fermi* and H.E.S.S. data points which are represented in red and blue, respectively. The red triangles are 3σ upper limits from *Fermi* data. The red dashed curve is the γ-ray bremsstrahlung, as predicted by our nonthermal radio spectrum with $\alpha = 0.25$ below 3.3 GHz and 1.7 above it. These values correspond to synchrotron spectrum of electrons with $p = 2\alpha+1 = 1.5$ and below 3.3 GHz and 4.4 above it. To convert from radio synchrotron flux to γ-rays, an equipartition field of 8 μG is selected, which is about a factor of two higher than 16 μG estimated from the cosmic-ray ionization rate (Figure 5(a)). In other words, the source volume and energetic electron density are similar to those used to estimate the ionization rate. One

difference is that the γ-ray flux from Sgr A* is not included here. Given that γ-ray flux depends on the product of neutral gas density and radio flux, we adjust the assumed hydrogen number density in the source volume to normalize the curve to give a reasonable fit to the data. We chose $n_H = 12.5$ cm^{-3} and a radio flux of 508 Jy at 325 MHz (using $n_H = 2.5$ cm^{-3} and a radio flux of 2450 Jy at 325 MHz could also give the same fit). Note that this could correspond to a higher density in a fraction of the source volume. A break in the radio spectrum reflecting the spectrum of γ-rays provides compelling evidence that the interaction of radio emitting GeV electrons with neutral gas is also responsible for production of GeV emission. The change in the spectral index can be attributed to rapid cooling of electrons at high energies.

The blue dashed power-law fit to the H.E.S.S. photon spectrum in Figure 12(a) is of the form $F_0(E/\text{GeV})^{-\Gamma}$ with $E^2 \times F_0 = (2.58 \pm 1.39) \times 10^{-5}$ MeV cm^{-2} s^{-1} and $\Gamma = 2.27 \pm 0.07$. Finally, the black solid curve is the sum of the two bremsstrahlung contributions, giving a reasonable fit to the H.E.S.S. and *Fermi* data. We assume that the emission at TeV energies is also produced by bremsstrahlung mechanism from an additional hard electron population with an $E^{-2.27}$ spectrum extending all the way from GeV to TeV. What is interesting about model fitted

Table 4
Parameters of the Fit to γ-ray Sources using *Fermi* and H.E.S.S. Data

Source	B (μG)	$n_{\rm H}$ (cm^{-3})	$F_{\rm 325\,MHz}$ (Jy)	$p1$	$p2$	$\nu_{\rm break}$ (GHz)	Flux (H.E.S.S.) (MeV cm^{-2} s^{-1})	Γ (H.E.S.S.)
GC diffuse	8	12.5	508	1.5	4.4	3.3	$(2.58 \pm 1.39) \times 10^{-5}$	2.27 ± 0.07
Sgr A	70	770	185	1.4	3.2	5	$(6.37 \pm 4.18) \times 10^{-6}$	2.20 ± 0.09
Sgr B2	30	2600	9	0.4	4.4	10	$(5.62 \pm 4.24) \times 10^{-6}$	2.19 ± 0.10
Radio Arc	40	450	156	2.4	2.8	20		
Sgr C	60	470	96	0.4	3.6	10		

H.E.S.S. spectrum is that it has a hard spectrum ($\Gamma = 2.27$), as is in the part of the modeled fitted *Fermi* spectrum ($\Gamma = 1.25$) that is not affected by cooling losses. We reconcile the GeV and TeV emission with similar spectrum in terms of a population of electrons that is young, thus producing γ-ray emission with a hard spectrum. The spectrum of the GeV emission showing a steep spectrum arises from an older generation of electrons that has experienced cooling.

As discussed above, the equipartition magnetic field of ∼15 μG gives longer lifetime for TeV particles to lose their energies. For example, for $E = 1$ TeV, $B = 15$ μG, $t_{\rm synch} \sim 800$ years, during which electrons will diffuse in the reservoir of molecular gas distributed in the central few hundred parsecs of the Galaxy, in the so-called CMZ (Morris & Serabyn 1996). We consider that the flux of TeV electrons inside molecular clouds streams freely along the magnetic field lines close to speed of light. This is because ion–neutral damping suppresses the magnetic fluctuations responsible for the diffusion.

Given the short lifetime of TeV electrons, the question arises as to what is responsible for resupplying these highly relativistic particles. One possibility for the production of TeV electrons is the site at which nonthermal Galactic center radio filaments interact with molecular clouds. There is at least one cloud in which nonthermal X-ray continuum emission has been detected at the edge of the cloud G0.11−0.11 (Wang et al. 2002b). Another possibility is that a source like Sgr A* is responsible for production of TeV electrons which then propagate through the CMZ of the Galactic center.

As a demonstration of the concept, model fitting of *Fermi* and H.E.S.S. emission from Sgr A and Sgr B2 as well *Fermi* emission from the radio arc near $l \sim 0°\!.2$ are shown in Figures 12(b)–(d), respectively. Table 4 shows the parameters of the fit to all these sources including Sgr C as well as the diffuse emission from the central $2° \times 1°$. Column 1 shows the source names and Columns 2–7 show the fit to *Fermi* data, whereas the last two columns give the observed H.E.S.S. flux and the photon index (Γ) required by the H.E.S.S. observations. The magnetic field (Column 2), the density of neutral gas (Column 3), radio flux at 325 MHz (Column 3), and the break frequency (Column 7) are adjusted in order to match the data. The indices of the broken power-law distribution of electrons $p1$ and $p2$ are shown in Columns 5 and 6. There is a degeneracy in the number density of neutral gas and the nonthermal radio flux. A more detailed measurement of the flux from individual sources and the possible contribution of electrons upscattering Galactic center background radiation will be given elsewhere. In this study, we use Table 4 as a demonstration of the concept that bremsstrahlung mechanism can explain the observed γ-ray emission. In the context of this picture, we predict that TeV electrons interacting with molecular gas are themselves the source of synchrotron emission. The synchrotron luminosity by TeV electrons is predicted to be 1 and 3×10^{38} erg s^{-1} for diffuse emission from the inner $2° \times$

$1°$ and Sgr B2, respectively. This should be observed in X-rays with the new generation of X-ray observatories like *Chandra*, *Suzaku,* and *XMM*. Another prediction of this model is that the population of young electrons with a hard spectrum should contribute 900 Jy to the radio flux at 330 MHz. These are robust predictions of the TeV electrons with a specific spectrum in X-rays that can be investigated in future studies.

5. CONCLUSIONS

We have explored different aspects of diffuse emission from the Galactic center in the context of cosmic-ray electrons' interaction with Galactic center clouds. We began by presenting γ-ray observations and data reductions using *Fermi* LAT, followed by studying the relativistic and the nonrelativistic components of nonthermal particles in the ISM of the Galactic center. We presented nonthermal radio flux over the inner $2° \times 1°$ of the Galactic center at four different radio frequencies. We used the reservoir of relativistic and nonrelativistic cosmic-ray electrons in the Galactic center region as seed particles interacting with neutral gas to determine the cosmic-ray ionization rate, molecular gas heating rate, and the production of Kα line and diffuse X-ray and γ-ray emission. The origin of high-energy X-ray and γ-ray emission was explained in the context of bremsstrahlung mechanism, as had previously been used to explain the origin of 6.4 keV line emission from neutral iron. In addition, we investigated the time variability of LECR flux by discussing that the cosmic-ray flux should vary on a short timescale because of ionization losses of electrons diffusing through a molecular cloud. The ionization losses of electrons are particularly dramatic at 100 keV which could diffuse for roughly 10 years in a medium with molecular density of 100 cm^{-3} before they lose most of their energy. Assuming that diffusion of LECR particles is not hindered by magnetic field fluctuations in molecular clouds, the fluorescent 6.4 keV line emission was predicted to vary on such a timescale unless there is constant acceleration of particles at these energies. Future studies will determine the importance of cosmic-ray irradiation model for individual Galactic center molecular clouds when compared to that of the X-ray irradiation model. Another characteristic that can place constraints on the applicability of these two models is to study the chemistry of the cosmic-ray-dominated region of the CMZ.

In summary, we explained the origin of γ-ray emission based on *Fermi* and the H.E.S.S. observations. The mechanism for the production of γ-ray emission is similar to that invoked to explain the production of Kα line emission except that high-energy particles are involved for production of bremsstrahlung γ-ray radiation. Another byproduct of the impact of cosmic rays with gas clouds is ionization losses suffered by interacting electrons with gas particles. The estimate of the ionization rate was compared with that measured from H_3^+ absorption lines. Lastly, cosmic rays heat molecular gas, increasing the temperature and

ionization fraction of molecular gas. The required cosmic-ray heating rate was estimated to explain an increasing molecular gas temperature in the Galactic center region. These physical processes placed constraints on the strength of the magnetic field, the cosmic-ray ionization rate and the cosmic-ray heating rate of molecular gas in the inner region of the Galaxy. Observed synchrotron emission from the Galactic center at radio wavelengths indicated a magnetic field of $\sim$15 μG and a large population of relativistic GeV electrons. The interaction of these electrons with neutral gas explained the GeV emission observed with *Fermi*. We were also able to explain the origin of the TeV emission and the Fe I Kα line emission at 6.4 keV which required high cosmic-ray ionization rate with some uncertainties related to the extrapolation of the electron spectrum to 10 keV and TeV energies.

REFERENCES

Abazajian, K. N. 2011, JCAP, 3, 10
Abdo, A. A., Ackermann, M., Ajello, M., et al. 2010a, ApJS, 188, 405 (1FGL)
Abdo, A. A., Ackermann, M., Ajello, M., et al. 2010b, ApJ, 722, 1303
Aharonian, F., Akhperjanian, A. G., Barres de Almeida, U., et al. 2008, A&A, 483, 509
Aharonian, F., Akhperjanian, A. G., Bazer-Bachi, A. R., et al. 2006, Natur, 439, 695
Atwood, W. B., Abdo, A. A., Ackermann, M., et al. 2009, ApJ, 697, 1071
Baganoff, F. K., Bautz, M. W., Brandt, W. N., et al. 2001, Natur, 413, 45
Boyarsky, A., Malyshev, D., & Ruchayskiy, O. 2011, PhLB, 705, 165
Camilo, F., Manchester, R. N., Gaensler, B. M., & Lorimer, D. R. 2002, ApJ, 579, L25
Chernyakova, M., Malyshev, D., Aharonian, F. A., Crocker, R. M., & Jones, D. I. 2011, ApJ, 726, 60
Chernyshov, D. O., Cheng, K. S., Dogiel, V. A., et al. 2012, PASJ, 64, 14
Crocker, R. M., Jones, D. I., Melia, F., Ott, J., & Protheroe, R. J. 2010, Natur, 463, 65
Dahmen, G., Hüttemeister, S., Wilson, T. L., et al. 1997, A&AS, 126, 197
Dalgarno, A., Yan, M., & Weihong, L. 1999, ApJS, 125, 237
Deneva, J. S., Cordes, J. M., & Lazio, T. J. W. 2009, ApJ, 702, 177
Duric, N., Gordon, S. M., Goss, W. M., Wiallefond, F., & Lacey, C. 1995, ApJ, 445, 173
Ferriere, K. 2009, A&A, 505, 1183
Fukuoka, R., Koyama, K., Ryu, S. G., & Tsuru, T. G. 2009, PASJ, 61, 593
Giveon, U., Sternberg, A., Lutz, D., Feuchtgruber, H., & Pauldrach, A. W. A. 2002, ApJ, 566, 880
Goldsmith, P. F., & Langer, W. D. 1978, ApJ, 222, 881
Goto, M., Usuda, T., Geballe, T. R., et al. 2011, PASJ, 63, 13
Goto, M., Usuda, T., Nagata, T., et al. 2008, ApJ, 688, 306
Gregory, P. C., & Seaquist, E. R. 1974, ApJ, 194, 715
Güsten, R., Walmsley, C. M., & Pauls, T. 1981, A&A, 103, 197
Hooper, D., & Goodenough, L. 2011, PhLB, 697, 412
Hüttemeister, S., Wilson, T. L., Henkel, C., & Mauersberger, R. 1993, A&A, 276, 445
Inui, T., Koyama, K., Matsumoto, H., & Tsuru, T. G. 2009, PASJ, 61, 241
Ishisaki, Y., Maeda, Y., Fujimoto, R., et al. 2007, PASJ, 59, 113
Johnson, S. P., Dong, H., & Wang, Q. D. 2009, MNRAS, 399, 1429
Johnston, S., Kramer, M., Lorimer, D. R., et al. 2006, MNRAS, 373, 6
Jones, P. A., Burton, M. G., Cunningham, M. R., et al. 2012, MNRAS, 419, 2961
Koyama, K., Maeda, Y., Sonobe, T., et al. 1996, PASJ, 48, 249
Koyama, K., Takikawa, Y., Hyodo, Y., et al. 2009, PASJ, 61, 255
Kushino, A., Ishisaki, Y., Morita, U., et al. 2002, PASJ, 54, 327
Lang, C. C., Goss, W. M., & Morris, M. 2002, AJ, 124, 2677

LaRosa, T. N., Brogan, C. L., Shore, S. N., et al. 2005, ApJ, 626, 23
Law, C. J., Yusef-Zadeh, F., Cotton, W. D., & Maddalena, R. J. 2008, ApJS, 177, 255
Lis, D. C., Serabyn, E., Zylka, R., & Li, Y. 2001, ApJ, 550, 761
Linden, T., Hooper, D., & Yusef-Zadeh, F. 2011, ApJ, 741, 95
Linden, T., Lovegrove, E., & Profumo, S. 2012, ApJ, 753, 41
Magnani, L., Zelenik, S., Dame, T. M., & Engebreth, B. 2006, ApJ, 636, 267
Maloney, P. R., Hollenbach, D. J., & Tielens, A. G. G. M. 1996, ApJ, 466, 561
Mauersberger, R., & Henkel, C. 1993, RvMA, 6, 69
Mezger, P. G., & Pauls, T. 1979, in IAU Symp. 84, The Large Scale Structure of the Galaxy, ed. W. Burton (Dordrecht: Reidel), 357
Monlinari, S., Bally, J., Noriega-Crespo, A., et al. 2011, ApJ, 735, 33
Morris, M. 2007, arXiv:astro-ph/0701050
Morris, M., & Serabyn, E. 1996, ARA&A, 34, 645
Morrison, R., & McCammon, D. 1983, ApJ, 270, 119
Muno, M. P., Baganoff, F. K., Bautz, M. W., et al. 2004, ApJ, 613, 326
Muno, M. P., Bauer, F. E., Baganoff, F. K., et al. 2009, ApJS, 181, 110
Muno, M. P., Bauer, F. E., Bandyopadhyay, R. M., & Wang, Q. D. 2006, ApJS, 165, 173
Murakami, H., Koyama, K., & Maeda, Y. 2001, ApJ, 558, 687
Neufeld, D. A., & Kaufman, M. J. 1993, ApJ, 418, 2
Neufeld, D. A., Lepp, S., & Melnick, G. J. 1995, ApJS, 100, 132
Nobukawa, M., Koyama, K., Tsuru, T. G., Ryu, S. G., & Tatischeff, V. 2010, PASJ, 62, 423
Nolan, P. L., Abdo, A. A., Ackermann, M., et al. 2012, ApJS, 199, 31 (2FGL)
Nord, M. E., Lazio, T. J. W., Kassim, N. E., et al. 2004, AJ, 128, 1646
Oka, T., Geballe, T. R., Goto, M., Usuda, T., & McCall, B. J. 2005, ApJ, 632, 882
Oka, T., Hasegawa, T., Sato, F., Tsuboi, M., & Miyazaki, A. 1998, ApJS, 118, 455
Park, S., Muno, M. P., Baganoff, F. K., et al. 2004, ApJ, 603, 548
Pierce-Price, D., Richer, J. S., Greaves, J. S., et al. 2000, ApJ, 545, 121
Ponti, G., Terrier, R., Goldwurm, A., Belanger, G., & Trap, G. 2010, ApJ, 714, 732
Reich, W. 1982, A&A, 113, 348
Reich, P., & Reich, W. 1986, A&AS, 63, 205
Rodriguez-Fernández, N. J., Martin-Pintado, J., Fuente, A., et al. 2001, A&A, 365, 174
Rudolph, A. L., Fich, M., Bell, F. R., et al. 2006, ApJS, 162, 346
Sawada, T., Hasegawa, T., Handa, T., et al. 2001, ApJS, 136, 189
Schlickeiser, R. 2003, Cosmic Ray Astrophysics (1st ed.; Berlin: Springler), 93
Schmidt, H. 1980, PhD thesis, Bonn Univ.
Simpson, J. P., Colgan, S. W. J., Cotera, A. S., et al. 2007, ApJ, 670, 1115
Strong, A. W., Moskalenko, I. V., & Reimer, O. 2004, ApJ, 613, 962
Strong, A. W., Orlando, E., & Jaffe, T. R. 2011, A&A, 534, 54
Sunyaev, R. A., & Churazov, E. 1998, MNRAS, 297, 1279
Sunyaev, R. A., Markevitch, M., & Pavlinsky, M. 1993, ApJ, 407, 606
Tatischeff, V., Decourchelle, A., & Maurin, G. 2012, A&A, 546, 88
Tawa, N., Hayashida, K., Nagai, M., et al. 2008, PASJ, 60, 11
Terrier, R., Ponti, G., Bélanger, G., et al. 2010, ApJ, 719, 143
Thompson, D. J., Bertsch, D. L., Dingus, B. L., et al. 1995, ApJS, 101, 259
Tsuboi, M., Handa, T., & Ukita, N. 1999, ApJS, 120, 1
Tsuboi, M., Tadaki, K., Miyazaki, A., & Handa, T. 2011, PASJ, 63, 763
Tsuboi, M. M., Ukita, N., & Handa, T. 1997, ApJ, 481, 263
Uchiyama, H., Nobukawa, M., Tsuru, T., Koyama, K., & Matsumoto, H. 2011, PASJ, 63, 903
Valinia, A., Tatischeff, V., Arnauld, K., Ebisawa, K., & Ramaty, R. 2000, ApJ, 543, 733
van der Tak, F. F. S., Belloche, A., Schilke, P., et al. 2006, A&A, 454, 99
Wang, Q. D., Gotthelf, E. V., & Lang, C. C. 2002a, Natur, 415, 148
Wang, Q. D., Lu, F., & Lang, C. C. 2002b, ApJ, 581, 1148
Wharton, R. S., Chatterjee, S., Cordes, J. M., Deneva, J. S., & Lazio, T. J. W. 2012, ApJ, 753, 108
Yaqoob, T., Murphy, K. D., Miller, L., & Turner, T. J. 2010, MNRAS, 401, 411
Yusef-Zadeh, F., Hewitt, J. W., & Cotton, W. 2004, ApJS, 155, 421
Yusef-Zadeh, F., Law, C., & Wardle, M. 2002, ApJ, 568, L121
Yusef-Zadeh, F., & Morris, M. 1987, AJ, 94, 1178
Yusef-Zadeh, F., Morris, M., & Chance, D. 1984, Natur, 310, 557
Yusef-Zadeh, F., Muno, M., Wardle, M., & Lis, D. C. 2007a, ApJ, 656, 847
Yusef-Zadeh, F., Nord, M., Wardle, M., et al. 2003, ApJ, 590, 103
Yusef-Zadeh, F., Roberts, D., & Wardle, M. 1997, ApJ, 490, L83
Yusef-Zadeh, Wardle, M., & Roy, S. 2007b, ApJ, 665, 123
Zarro, D. M., Dennis, B. R., & Slate, G. L. 1992, ApJ, 391, 865